# Chronostratigraphy of two Late Pleistocene loess-palaeosol sequences in the Rhône Valley (southeast France)

Mathieu Bosq, Sebastian Kreutzer, Pascal Bertran, Jean-Philippe Degeai, Pauline Dugas, Annette Kadereit, Philippe Lanos, Olivier Moine, Nora Pfaffner, Alain Queffelec, et al.

# Chronostratigraphy of two Late Pleistocene loess-palaeosol sequences in the Rhône Valley (southeast France)

Mathieu Bosq[1,*], Sebastian Kreutzer[2,3], Pascal Bertran[1,4], Jean-Philippe Degeai[5], Pauline Dugas[1,6], Annette Kadereit[7], Philippe Lanos[2,8], Olivier Moine[9], Nora Pfaffner[10], Alain Queffelec[1], Daniela Sauer[10]

[1] PACEA, UMR 5199 CNRS - Université Bordeaux, Bâtiment B2, allée Geoffroy Saint Hilaire, 33615 Pessac, France

[2] IRAMAT-CRP2A, UMR 5060 CNRS - Université Bordeaux Montaigne, Maison de l'Archéologie, 33607 Pessac, France

[3] Geography & Earth Sciences, Aberystwyth University, Aberystwyth, SY23 3DB, Wales, United Kingdom

[4] Inrap, 140 avenue du Maréchal Leclerc, 33130 Bègles, France

[5] ASM, UMR 5140 CNRS - Université de Montpellier III, route de Mende, 34199 Montpellier, France

[6] Adera, PACEA-Transfert Sédimentologie & Matériaux. 162 avenue du Docteur Schweitzer 33600 Pessac

[7] Heidelberg Luminescence Laboratory, Institute of Geography, University of Heidelberg, Germany

[8] Géosciences Rennes – Université de Rennes I, 35042 Rennes, France

[9] LGP, UMR 8591 CNRS - Université Paris I Panthéon-Sorbonne/Université Paris-Est-Créteil-Val-de-Marne (UPEC), place Aristide Briand, 92195 Meudon, France

[10] Institute of Geography, University of Göttingen, Germany

## ABSTRACT

A sedimentological and chronostratigraphical investigation was carried out on two loess sections located in the Mediterranean area in southeast France along the Rhône River (Lautagne) and the lower reach of a tributary of the Rhône River (Collias). High-resolution sampling (5-20 cm) for magnetic susceptibility, grain size distribution (including non-parametric end-member modelling), colour reflectance and geochemistry was performed. The chronology was based on luminescence dating of quartz grains and radiocarbon dating of small gastropod shells, coupled with hierarchical Bayesian modelling. The Collias section (~8 m thick) records the whole last climatic cycle. It comprises a thick red basal pedocomplex S1 developed during the Last Interglacial and the Early Glacial, similar to that observed elsewhere in southern and southeastern Europe. Loess deposition occurred during the Lower (L1L2) and the Upper Pleniglacial (L1L1). It was interrupted by soil formation during the Middle Pleniglacial, of which a brown Bwk horizon has been preserved (L1S1). By contrast, the ~5 m thick Lautagne section provides a detailed record of the Upper Pleniglacial. Weakly developed hydromorphic soils are correlated with the Greenland Interstadials GI-4 to GI-2, while the main period of coarse loess sedimentation corresponds to the Greenland Stadials GS-5 to GS-2. At a regional scale, the time of loess deposition ranges between 38.5 ka and 12 ka, with a peak at ~28–24 ka, overlapping with the maximal advance of the Alpine Ice Sheet (AIS). This strongly suggests that regional glacier dynamics was the main driver of loess sedimentation.

*Keywords:* loess; southeast France; chronology; geochemistry; grain-size distribution; Last Glacial.

## 1. Introduction

Loess deposits are widespread across the European continent and constitute key terrestrial archives for reconstructing the palaeoenvironments of the last climatic cycle. During the Last Glacial, drastic reduction of the vegetation cover, increase in wind intensity and decrease in precipitation favoured the global emission of dust (Hopcroft et al., 2015; Lunt and Valdes, 2002; Mahowald et al., 2006; Schaffernicht et al., 2020). Loess accumulated at the periphery of the Eurasian Ice-Sheet (EIS) and on the banks of major rivers draining mountain ice caps. Past advances of luminescence-dating methods, such as optically simulated luminescence (OSL, Huntley et al., 1985) on quartz, and infrared stimulated luminescence (IRSL, Hütt et al., 1988) or post-IR IRSL (pIRIR, Thomsen et al., 2008) on feldspar and polymineral grains, have enabled the establishment of a robust chronological framework of the phases of loess accumulation and soil formation (e.g., Frechen and Schirmer, 2011; Fuchs et al., 2013; Guérin et al., 2017; Kreutzer et al., 2012; Lomax et al., 2014; Moska et al., 2019, 2015; Sauer et al., 2016; Thiel et al., 2011; Zens et al., 2018; Zöller et al., 2013). Simultaneous improvements of radiocarbon dating by Accelerator Mass Spectrometry (AMS) made it possible to analyse small charcoal pieces and carbonate biomineralisations (e.g., small terrestrial gastropod shells, earthworm calcite granules) and also greatly contributed to support and refine previous loess chronology in some regions (e.g., Moine et al., 2017; Újvári et al., 2016b). Overall, the progress in dating accuracy over the past decades highlighted the impact of millennial climate variations such as Dansgaard-Oeschger (D-O) cycles upon loess sedimentation in Europe.

Yet, because of its patchy distribution and variable thickness, peri-Mediterranean loess remains poorly documented except for some publications (Calvo et al., 2016; Profe et al., 2016; Wacha et al., 2018; Costantini et al., 2018). Recent studies in the Po plain in Italy (Cremaschi, 1990; Cremaschi et al., 2015; Zerboni et al., 2015) and Croatia (Wacha et al., 2018), as well as in the Ebro (Boixadera et al., 2015) and Tagus basins (Wolf et al., 2019, 2018) in Spain suggested, however, that Pleistocene loess covers considerable areas in peri-Mediterranean regions. Last Glacial loess is also widespread in the Rhône Valley, southeast France (Bosq et al., 2018, 2020 and references therein). These deposits have specific characteristics when compared to loess from the North-European Loess Belt (NELB), including a coarser texture (main grain-size mode around 60 μm), polymodal grain-size distribution, locally great thickness but discontinuous spatial distribution, high carbonate content and abundant synsedimentary bioturbation. Such pattern is assumed to reflect the capture of particles in saltation and short-term suspension by shrub vegetation close to the fluvial sources, in a milder climate than that of the North European plains. Geochemical analyses show that loess deposits derived from the rivers (Rhône, Rhine, Danube and Po) draining the Alpine Ice Sheet (AIS) have a similar, Ca-rich composition (cf. Bosq et al., 2020). They are referred here as to “perialpine loess”.

This paper has the following objectives: (1) high-resolution multi-proxy analysis of two sections (Collias and Lautagne) representative of the loess-palaeosol sequences of the Rhône Valley, southeast France, (2) development of an accurate chronological framework using a hierarchical Bayesian model based on OSL and AMS $^{14}$C ages of the section of Lautagne, and

(3) comparison of the chronology of loess deposition with AIS fluctuations and the North Greenland Ice Core Project (NGRIP) ice record.

## 2. Materials and methods

### 2.1. Study sites, description and sampling

The sequence Collias (43.953°N; 4.466°E; 100 m a.s.l.) is located on the left bank of the Gardon River, upstream of its confluence with the Rhône (**Fig. 1A, 1B**). In this area, loess deposits reaching locally 10 m thickness were recognised in the 1950s and 1960s (Bonifay, 1962; Mazenot, 1956; Tricart, 1952). Loess overlies Lower Miocene molasse (noted m1v on the 1:50,000 geological map, http://infoterre.brgm.fr/) and extends from the foot of a Lower Cretaceous (n4-5U) limestone massif to the alluvial plain of the Alzon river (**Fig. 1C**). A previous study has demonstrated that the geochemical composition of alluvium from the Gardon River (as well as all the rivers from the French Massif Central) differs from that of loess of the Rhône Valley, including the Collias samples (Bosq et al., 2020). The geochemical data also revealed that the dust was mainly supplied by the bed of the Rhône River (at that time a braided river, carrying the sediment loaded meltwater of the Alpine (and Jura) glaciers). Bonifay (1962) distinguished two loess generations and assigned them to the Last Glacial ("Series I") and the Penultimate Glacial ("Series II"). According to the same author, the two generations are separated by an erosional discontinuity attributed to the Last Interglacial. The studied section is a sub-vertical outcrop created during the construction of a forest road. A Mediterranean climate with low rainfall (Mean Annual Precipitation, MAP = 763 mm), hot summers ($T_{max}$≥22°C) and relatively high annual temperatures (Mean Annual Temperature, MAT = 15.2 °C) characterises the area (meteorological data for the period 1981–2010; https://donneespubliques.meteofrance.fr).

The sequence Lautagne (44.904°N; 4.897°E; 177 m a.s.l.) is located south of Valence on the left bank of the Rhône (**Fig. 1D**), on a river terrace (Fw) attributed to the Middle Pleistocene (Mandier, 1988), showing a well-developed rubified palaeosol. Two test pits were dug during archaeological excavations led by the *Institut national de recherches archéologiques préventives* (Inrap) (see **Fig. A1** in **Appendix A)**. The fluvial gravel is buried by loess, reaching a thickness of up to 5 m (profile A) and gradually decreasing towards the edges of the plateau (profile B). Lautagne is located at the transition between a semi-continental climate to the north and a Mediterranean climate to the south, with a MAP = 923 mm and a MAT = 13.3 °C.

Excavation and manual cleaning of the sections created successive vertical panels (1 m to 2 m high and > 1 m wide) separated by steps, making description and sampling easier. The lithofacies codes were taken from Miall (1996), and the soil horizons were classified according to the FAO Guidelines for Soil Description (FAO, 2006) and the World Reference Base for Soil Resources (IUSS Working Group WRB, 2015). Samples were collected for magnetic susceptibility, grain-size distribution and colourimetry at 5 cm depth-resolution, and for geochemistry at 20 cm depth-resolution. In total, 164 (Collias) and 98 (Lautagne) samples were collected and analysed (**Figs. 2** and **3**). In addition, eight blocks of sediment (15 cm x 10

cm x 7 cm) were extracted from each section for thin section preparation according to the method described by Guilloré (1980). The micromorphological description of the samples was carried out according to the recommendations of Stoops (2003).

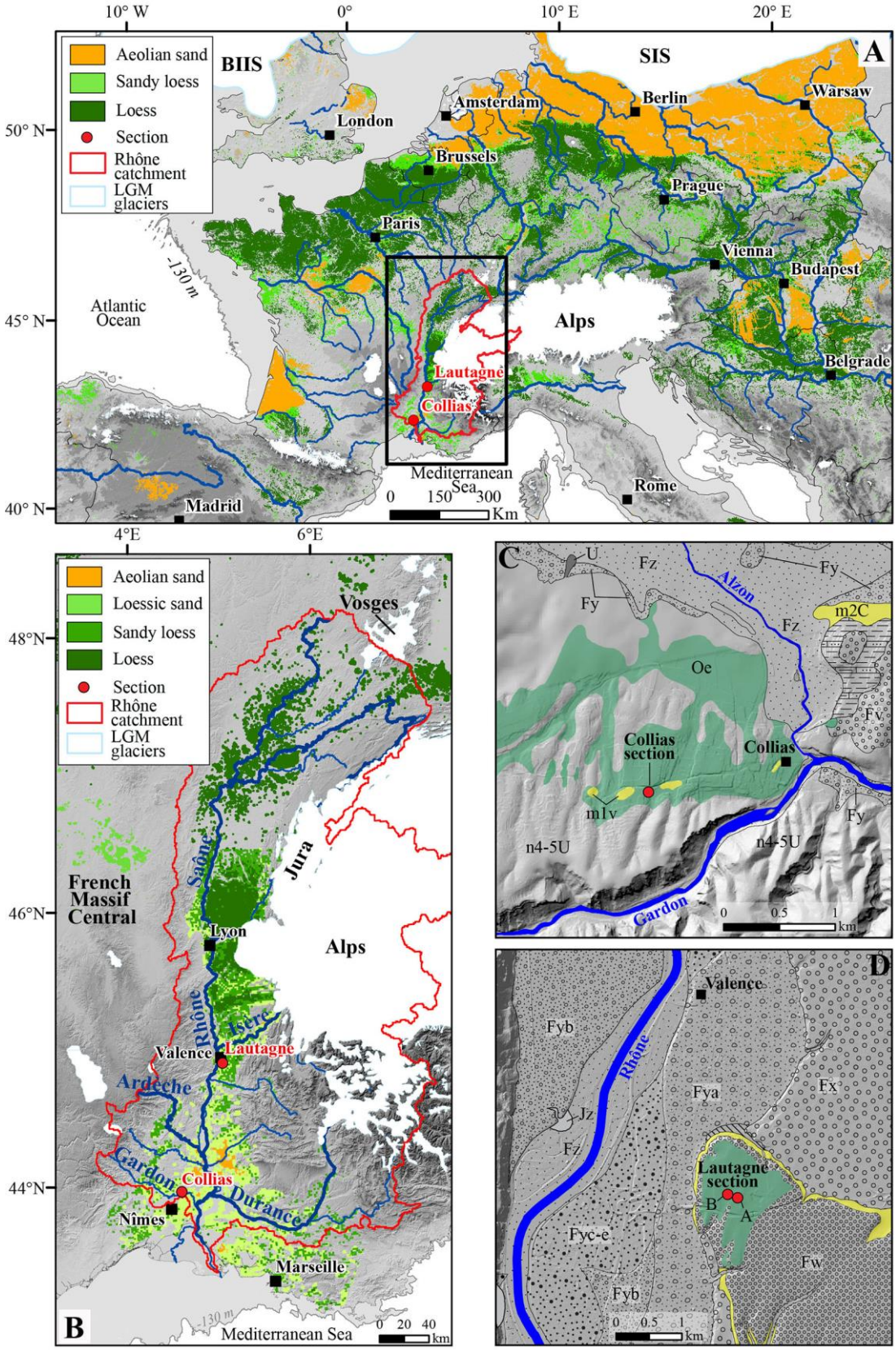

**Fig. 1**: A) Map of aeolian deposits in Western Europe from Bertran et al. (2016) with additional data from Bosq et al. (2018) and Lindner et al. (2017), showing the location of the sections studied in the Rhône Valley and within the Rhône catchment (red line). The British-Irish Ice Sheet (BIIS) and Scandinavian Ice Sheet (SIS) are from Hughes et al. (2016). The Alpine Ice Sheet (AIS) and other LGM glaciers are from Ehlers and Gibbard (2004). Sea-level drop to 130 m below sea level during the LGM is assumed (Lambeck et al., 2014). Palaeocoastlines are from Zickel et al. (2016). The map is based on a Digital Elevation Model (DEM) (ETOPO1; Amante and Eakins, 2009), ETRS89-LAEA projected geographic coordinate system. B) Spatial distribution of aeolian deposits in the study area (Bosq et al. 2018). C, D) Close-up maps of the Collias (C) and Lautagne (D) areas, based on a DEM with 5 m resolution from RGE ALTI® (http://professionnels.ign.fr). The geological formations were redrawn from the 1:50,000 geological map (http://infoterre.brgm.fr). Abbreviations: Fz=Holocene floodplain, Fy, Fyc-e, Fyb, Fya, Fw, Fv=Pleistocene terraces, Jz=alluvial fans, m1v/m2C=Miocene molasses (yellow), n4-5U=Cretaceous limestone, Oe=loess (green), U=travertine.

### 2.2. Bulk magnetic susceptibility

Measurements of the specific-mass magnetic susceptibility ($\chi$) of each sample were performed in the laboratory using a Bartington MS2B at room temperature. The results are expressed in $10^{-6}$ $m^3$/kg. The dry, bulk sedimentary material was homogenised and compressed in a 10 ml plastic cylinder. $\chi$ values reflect the concentration of minerals with ferrimagnetic properties (mainly magnetite and maghemite). Nevertheless, this proxy can be biased by the grain-size distribution of magnetic grains. Indeed, ferrimagnetic grains of the superparamagnetic grain-size (SP, <0.03 µm) have a significantly higher $\chi$ than single-domain (SD, >0.03 µm) or multi-domain (MD, >~10 µm) particles (Thompson and Oldfield, 1986). The use of the frequency dependent magnetic susceptibility ($\chi_{FD}$) partially resolves these limitations (Obreht et al., 2019). This parameter is the relative difference between the mass magnetic susceptibility values measured at low frequency (0.46 kHz) and high frequency (4.65 kHz) ($\chi_{LF}$ and $\chi_{HF}$ respectively). $\chi_{FD}$ (expressed in %) was calculated as follows:

$$\chi \quad \frac{\chi_{LF} \quad \chi_{HF}}{\chi_{LF}}$$

$\chi_{FD}$ is a measure of the relative contribution of SP ferrimagnetic particles approaching the SP-SD threshold that are formed exclusively *in-situ* (e.g., Dearing et al., 1996; Maher and Taylor, 1988). Therefore, $\chi_{FD}$ is considered to be a very efficient proxy for determining the weathering intensity (Buggle et al., 2014; Dearing et al., 1996).

### 2.3. Grain-size distribution and end-member modelling

The samples for grain-size distribution analysis were processed using a Horiba LA-950 laser particle size analyser. After passing the samples through a 2 mm sieve to remove the coarser fraction (secondary carbonate concretions, shells, gravels and roots), the sample pre-treatment included suspension in sodium hexametaphosphate (5 g/l) and hydrogen peroxide (35%) at room temperature for 12 h. As recommended by Schulte et al. (2016), the carbonates were not removed. Then, the suspension was subjected to 60 s ultrasonification to achieve optimal dispersion. The Mie solution to Maxwell's equation provided the basis for calculating the particle size distribution (ISO, 2009; Jones, 2003), using a refractive index of 1.333 for water and 1.55i – 0.01i for the particles (see Appendix of Sitzia et al., 2017 for details on the procedure). The upper limit of clay measured by laser granulometry was set at 8 µm after

calibration by the sieve-pipette method as described in Bosq et al. (2018). Finally, the *Grain Size Index* (GSI) defined by Antoine et al., 2009a was calculated. The GSI is the ratio between coarse silt (52–26 µm) and fine silt plus clay (< 26 µm).

Grain-size distribution can provide key information on the provenance, mechanisms and/or distance of transport, and the depositional environment of sediments (e.g., Bagnold and Barndorff-Nielsen, 1980; Újvári et al., 2016a; Vandenberghe, 2013). Two approaches have been developed to decompose grain-size distributions and to quantify dominant subpopulations in aeolian sediments: (i) parametric curve fitting using a mixture of log-normal (Bosq et al., 2018; Qin et al., 2005) or Weibull distribution functions (Sun et al., 2002) and (ii) non-parametric end-member modelling analysis (EMMA) (Dietze et al., 2012; Vriend and Prins, 2005; Weltje, 1997; Weltje and Prins, 2007; Dietze and Dietze, 2019). In this study, the EMMA approach was applied using the MATLAB® GUI software of AnalySize developed by Paterson and Heslop (2015). The main advantage of this method is that it describes an entire grain-size dataset as a mixture of distinct unimodal or polymodal subpopulations (Dietze et al., 2012; Weltje, 1997; Weltje and Prins, 2007). The analysis was arbitrarily restricted to the grain-size class [>1 µm to <678 µm] to eliminate a large number of zeros that cause numerical instabilities in the treatment. The determination coefficient $R^2$ was calculated to identify the minimum number of end-members (EMs) (q) necessary for correct statistical interpretation. Following this principle of parsimony, an EM model with q = 3 was chosen as it allowed a significant improvement of $R^2$ from 2 to 3 Ems while the improvement was reduced from 3 to 4 EMs (see **Fig. A2**). This model explains 97.8% of the total variance of the dataset. Then, the distribution of each EM was split into different populations by the parametric curve fitting method using the R (R Core Team, 2019) package 'mixdist' (Macdonald and Du, 2015) to identify the different modes. A log-normal distribution was used.

### 2.4. Spectrocolourimetry

The colour of moist sediments was determined in the field using the Munsell soil colour chart (Munsell, 2000). The colour of the dry, crushed and homogenised samples was then measured in the laboratory using an Avantes AvaSepc-2048 fibre-optic spectrometer. The instrument was equipped with an optic fibre probe (1 mm diameter) that was placed at a short distance (2 mm) from the smooth surface of the sample. An AvaLight-Hal was used as the light source, and the equipment was calibrated with a white reference sample (Halon D65). Three measurements per sample were performed, and the average was then calculated. The spectral information obtained was converted into the CIELAB (L*, a*, b*) system (CIE, 1976) using Avasoft 7.5 software. The variable L* indicates the lightness on a scale from 0 (black) to 100 (white) while the variables a* and b* express the colour in chromatic coordinates on the red-green (positive a* - negative a*) and blue-yellow (positive b* - negative b*) scales.

Colour differences between yellowish loess and reddish-brown palaeosols are mainly a consequence of goethite and hematite concentrations (Ji et al., 2001). The chromaticity values a* is closely related to the relative abundance of pedogenic hematite (e.g., Lukić et al., 2014).

### 2.5. Geochemical analysis

The sediment was passed through a 100 µm sieve to remove coarse sand grains, ferruginous nodules, carbonate concretions and other debris such as calcified roots, mollusc shells and earthworm calcite granules, which may disturb the results of the geochemical analysis. The fine fraction <100 µm was ground and pressed into pellets for X-ray fluorescence (ED-XRF) using a portable Bruker Tracer 5i. Two measurements were taken under vacuum on all samples, one at 15 kV and 100 µA for 300 s without a filter to quantify light elements (Na, Mg, Al, Si, P, K, Ti, V, Cr, Mn, Fe) and the other at 50 kV and 35 µA for 120 s with the Cu75, Ti25, Al200 filter for heavy elements (Ni, Zn, Ga, As, Rb, Sr, Y, Zr, Nb, Ba, La, Ce, Nd, Hf, Pb, Th) and Ca. The instrument was calibrated by use of the CloudCal v3.0 application (Drake, 2018; https://github.com/leedrake5/CloudCal), using the algorithm proposed by Lucas-Tooth and Price (1961). The calibration was performed using the geochemical composition of 43 loess and alluvial samples determined by Inductively Coupled Plasma-Atomic Emission Spectroscopy (ICP-AES) and ICP-Mass Spectrometry (ICP-MS) at the Service d'Analyse des Roches et des Minéraux (CRPG-SARM, Nancy, France) according to a previously published methodology (Bosq et al., 2020). Only the elements for which the determination coefficient $R^2$ between the analytical results of the ED-XRF and the ICP-AES/ICP-MS was greater than 0.7 were considered (cf. **Figs. A3 and A4**).

A wide variety of geochemical indices based on major and trace elements has been developed to study dust provenance, grain-size sorting and weathering intensity in European loess (cf. Bosq et al., 2020). For the purposes of this study, we focused on the following element ratios and indices: Ti/Al, Si/Al, CPA, Rb/K, Fe/Al, and Ca/Al. Al is considered here as the invariant element. Ti, mainly in the form of oxides (anatase, brookite, rutile), forms inclusions in mafic minerals, especially biotite, which is concentrated in the fine fraction (Young and Nesbitt, 1998). The Ti/Al ratio is used here as an indicator of the homogeneity of the sedimentary source (Sheldon and Tabor, 2009). The Si/Al ratio is sensitive to grain-size sorting since Si-rich tectosilicates (quartz, feldspars) are over-represented in the coarser fractions, whereas Al-rich phyllosilicates constitute a large part of the finer fractions (Bouchez et al., 2012; Guo et al., 2018; Liang et al., 2013). Weathering indices are based on the selective removal of soluble and mobile elements (particularly alkali and alkaline earth elements) during pedogenesis (Buggle et al., 2011; Nesbitt and Young, 1982). The weathering intensity of silicates was quantified using the *Chemical Proxy of Alteration* (CPA) (in molar proportion):

$$CPA = 100 \times \frac{Al}{\quad}$$

CPA (originally called Chemical Index of Weathering (CIW') by Cullers, 2000) was considered a proxy for plagioclase weathering intensity by Buggle et al. (2011). The CPA is particularly adapted to poorly weathered sediments since weathering first impacts plagioclases rather than K-feldspars (Nesbitt and Young, 1989). Besides the CPA, the K/Rb ratio was used to estimate the weathering intensity of K-bearing minerals (Nesbitt et al., 1980; Wronkiewicz and Condie, 1990), since K is more mobile than Rb due to its smaller ionic radius. Rb is hosted by K-feldspars, micas and clay minerals (Heier and Billings, 1970;

Nesbitt et al., 1980). As Ca is essentially hosted by calcite, the Ca/Al ratio allows to evaluate the depth distribution of calcite along the sequence, in particular the secondary precipitation of calcite of pedogenic origin at certain profile depths, provided that the contents of plagioclases and primary calcium carbonate are roughly constant across the profile. The Fe/Al ratio is used to distinguish the B horizons of soils that are relatively enriched in Fe, due to the formation of immobile iron oxides such as magnetite ($Fe_3O_4$), hematite ($Fe_2O_3$) and goethite (FeO(OH)) (Reimann et al., 2014).

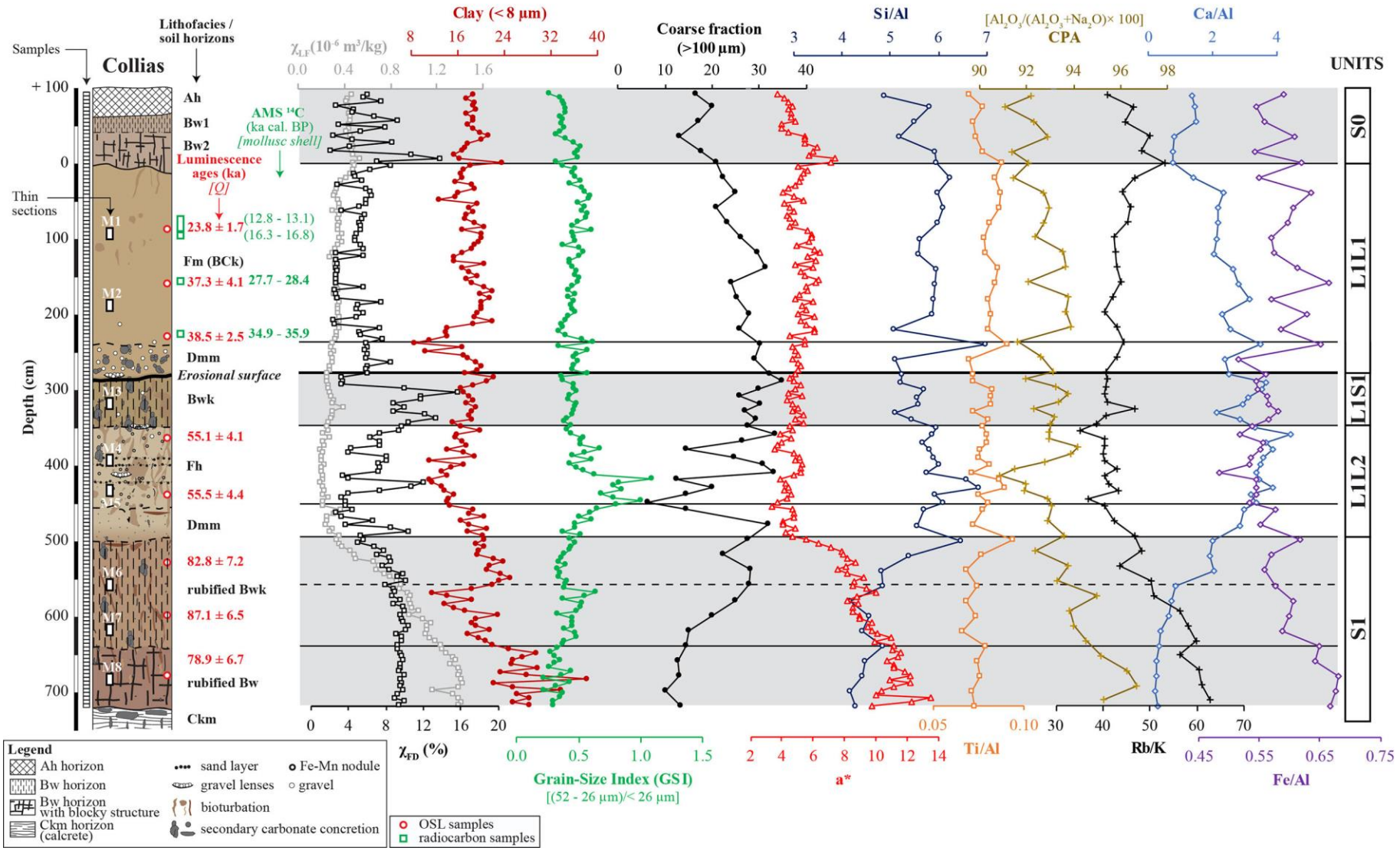


**Fig. 2**: Detailed stratigraphy of the Collias section with the locations of the samples for sedimentological and micromorphological analyses. Curves: low-frequency mass-specific magnetic susceptibility ($\chi_{LF}$) expressed in $10^{-6}$ $m^3$/kg, frequency dependent magnetic susceptibility ($\chi_{FD}$) expressed in %, grain-size parameters (clay, GSI, coarse fraction), colour reflectance (a*), geochemical ratios (Si/Al, Ti/Al, CPA, Rb/K, Ca/Al, Fe/Al). Details on luminescence dating results (red) are provided in **Table 1** and on radiocarbon dating results (green) in **Table 2**. The grey bars indicate soil formation.

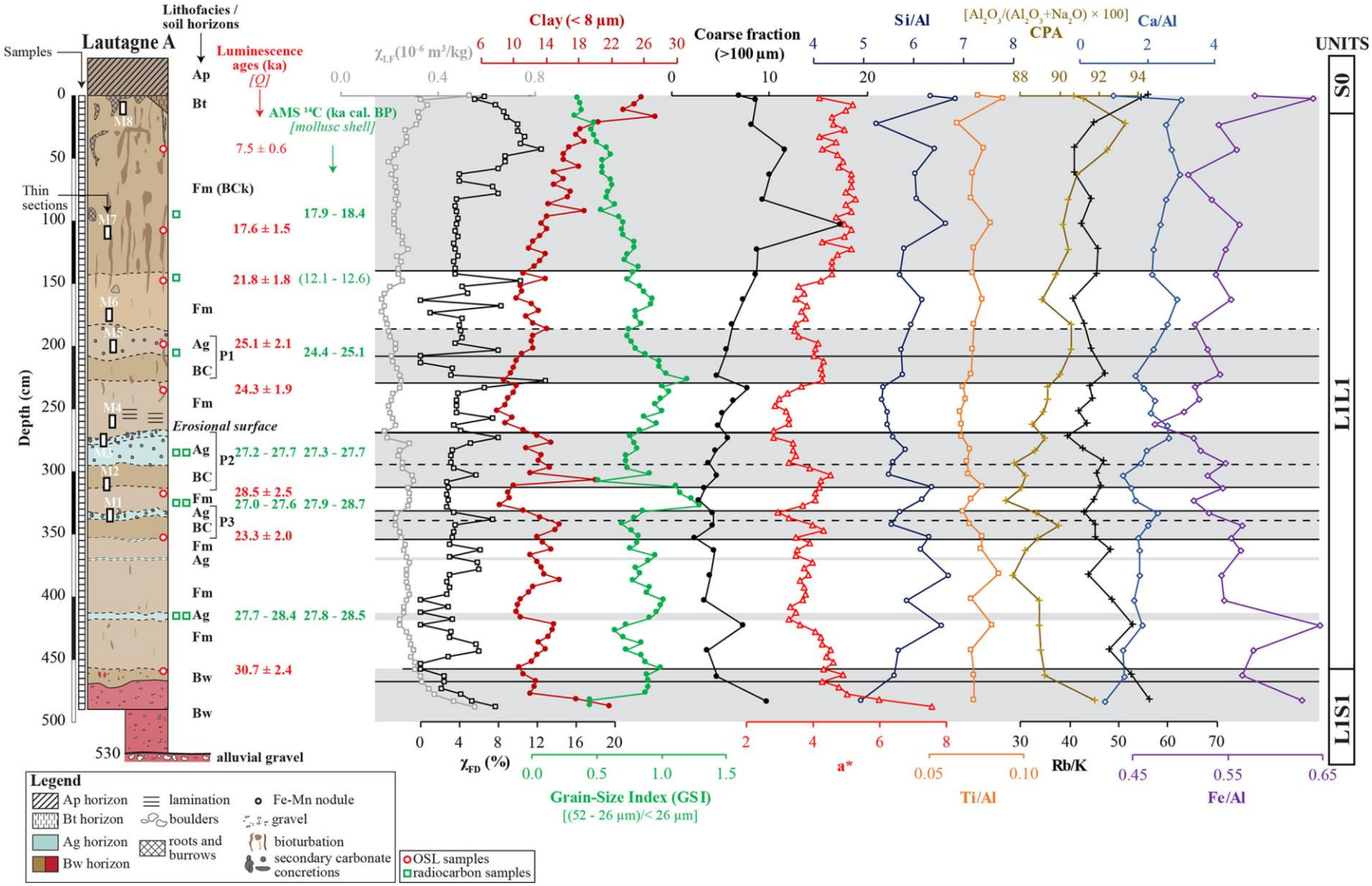


**Fig. 3**: Detailed stratigraphy of the Lautagne section (Lautagne A) with the locations of the samples for sedimentological and micromorphological analyses. Curves: low-frequency mass-specific magnetic susceptibility ($\chi_{LF}$) expressed in $10^{-6}$ $m^3$/kg, frequency dependent magnetic susceptibility ($\chi_{FD}$) expressed in %, grain-size parameters (clay, GSI, coarse fraction), colour reflectance (a*), geochemical ratios (Si/Al, Ti/Al, CPA, Rb/K, Ca/Al, Fe/Al). Details on luminescence dating results (red) are provided in **Table 1** and on radiocarbon dating results (green) in **Table 2**. The grey bars indicate soil formation.

## 2.6. Chronological data

### *2.6.1 Luminescence dating*

The two sites Lautagne and Collias were subjects to luminescence dating at the IRAMAT-CRP2A (Université de Bordeaux-Montaigne) between 2016 and 2019. In both cases, the samples were extracted under daylight using steel cylinders. In total, we prepared 18 samples (10 from Lautagne, including 8 from section A and 2 from section B, and 8 samples from Collias) to extract the fine-grain (4–11 µm) (Lautagne) and coarse-grain (90–200 µm) (Collias) quartz fractions (see **Table 1**). Additionally, we extracted coarse-grain quartz separates for Lautagne and the K-feldspar fraction of 2 samples from Collias for cross-checks. The sample preparation was supported by the luminescence laboratories of the Justus-Liebig University Giessen (Germany) and the University of Bayreuth (Germany), following routine luminescence dating preparation methods (e.g., Preusser et al., 2008). The quartz samples were subjects to OSL measurements, applying the single-aliquot regenerative (SAR) dose protocol (Murray and Wintle, 2000). Equivalent doses ($D_e$) were measured on Freiberg Instruments *lexsyg research* luminescence readers (Richter et al., 2013), and the data analysis was performed with the R (R Core Team, 2019) package 'Luminescence' (Kreutzer et al., 2012b, 2020). We applied the average dose model (Guillaume Guérin et al., 2017) to samples from Lautagne and the 'baSAR' approach (Combès et al., 2015; Mercier et al., 2016) to samples from Collias to calculate the average dose and the central dose respectively, and their corresponding standard errors. Dose-rate measurements relied on *in situ* gamma-dose rate measurements at Lautagne (cf. Løvborg and Kirkegaard, 1974; Mercier and Falguères, 2007) and high-resolution gamma-ray spectrometry procedure at the IRAMAT-CRP2A, cf. Guibert and Schvoerer, 1991). In addition, we measured U, Th, K concentrations for all samples from both sites. The online calculator *DRAC* (Durcan et al., 2015) in version 1.2 provided the final luminescence ages. We show full details of the luminescence dating, including further references, in **Appendix B**.

### *2.6.2. AMS radiocarbon dating*

Last Glacial loess-palaeosol sequences (LPS) in southeast France lack organic remains that can be easily dated by the radiocarbon method. To overcome this problem, recent studies have been undertaken, which have shown that calcitic biomineralisations such as terrestrial gastropod shells or earthworm granules can be used to obtained a precise chronology (e.g., Moine et al., 2017; Újvári et al., 2016b). The advantage of this approach is that these carbonates are relatively abundant in loess. In the past, mollusc shells have often been avoided for dating because large taxa incorporate carbon from the substrate, which causes apparent radiocarbon-age increases up to several thousand years (Evin et al., 1980; Goodfriend and Stipp, 1983). However, several studies have shown that this effect is much more limited and generally negligible for small (<10 mm) gastropods (Brennan and Quade, 1997; Pigati et al., 2010).

Ten litres of bulk sediment have been wet sieved on a 425-µm mesh. Then, gastropod shells and earthworm calcite granules were cleaned by ultrasonic treatment and were analysed in the following laboratories: (i) the AMS facilities of the Hertelendi Laboratory of Environmental

Studies, Institute for Nuclear Research at Debrecen (Hungary) (Molnár et al., 2013); (ii) the Radiocarbon dating centre at Lyon (France) within the framework of the ARTEMIS programme and (iii) the Centre for Isotope Research at Groningen (Netherlands) (Dee et al., 2020). Conventional radiocarbon ages were calibrated to calendar ages with the *IntCal13* calibration curve (Reimer et al., 2013), using the software *Calib* in version 7.0.4 (Stuiver and Reimer, 1993). Calibrated ages are reported as age ranges at the 2 sigma (σ) confidence level (95.4%).

**Table 1**

Final dose rates, equivalent doses ($D_e$) and luminescence age values of the Collias and Lautagne A sections. Uncertainties are quoted as 1σ, rounded to one digit.

Final ages used for this study are quoted in bold numbers. For more details, see the **Appendix B.**

| Sample name | Laboratory code | Mineral | Depth | External dose rate (water corr.) | | | Internal dose rate | | $\dot{D}_{cosm.}$ | $\dot{D}_{ext.}$ | $\dot{D}_{int.}$ | $\dot{D}_{env.}$ | $D_e$ | Age | Posterior calib. date ka b2k (HPD, 95%) | |
|---|---|---|---|---|---|---|---|---|---|---|---|---|---|---|---|---|
| | | | | $\dot{D}_\alpha$ | $\dot{D}_\beta$ | $\dot{D}_\gamma$ | $\dot{D}_\alpha$ | $\dot{D}_\beta$ | | | | | | | | |
| | | | (m) | (Gy ka$^{-1}$) | (Gy ka$^{-1}$) | (Gy ka$^{-1}$) | (Gy ka$^{-1}$) | (Gy ka$^{-1}$) | (Gy ka$^{-1}$) | (Gy ka$^{-1}$) | (Gy ka$^{-1}$) | (Gy ka$^{-1}$) | (Gy) | (ka) | From - To | |
| Collias BAY | BDX21322 | Q | 0.90 | 0.0 ± 0.0 | 1.1 ± 0.1 | 0.8 ± 0.0 | 0.0 ± 0.0 | 0.0 ± 0.0 | 0.3 ± 0.0 | 2.2 ± 0.1 | 0.0 ± 0.0 | 2.2 ± 0.1 | 51.4 ± 2.6 | **23.8 ± 1.7** | - | |
| Collias BAY | BDX21323 | Q | 1.60 | 0.0 ± 0.0 | 1.0 ± 0.1 | 0.8 ± 0.0 | 0.0 ± 0.0 | 0.0 ± 0.0 | 0.2 ± 0.0 | 1.9 ± 0.1 | 0.0 ± 0.0 | 1.9 ± 0.1 | 71.6 ± 7.0 | **37.3 ± 4.1** | - | |
| Collias BAY | BDX21324 | Q | 2.30 | 0.0 ± 0.0 | 1.0 ± 0.1 | 0.8 ± 0.0 | 0.0 ± 0.0 | 0.0 ± 0.0 | 0.2 ± 0.0 | 1.9 ± 0.1 | 0.0 ± 0.0 | 1.9 ± 0.1 | 72.0 ± 3.1 | **38.5 ± 2.5** | - | |
| Collias BAY | BDX21325 | Q | 3.65 | 0.0 ± 0.0 | 0.9 ± 0.0 | 0.7 ± 0.0 | 0.0 ± 0.0 | 0.0 ± 0.0 | 0.1 ± 0.0 | 1.7 ± 0.1 | 0.0 ± 0.0 | 1.7 ± 0.1 | 94.7 ± 5.3 | **55.1 ± 4.1** | - | |
| Collias BAY | BDX21326 | Q | 4.4 | 0.0 ± 0.0 | 1.0 ± 0.1 | 0.8 ± 0.0 | 0.0 ± 0.0 | 0.0 ± 0.0 | 0.1 ± 0.0 | 1.9 ± 0.1 | 0.0 ± 0.0 | 1.9 ± 0.1 | 106.8 ± 6.7 | **55.5 ± 4.4** | - | |
| Collias BAY | BDX21327 | Q | 5.30 | 0.0 ± 0.0 | 1.1 ± 0.1 | 0.9 ± 0.0 | 0.0 ± 0.0 | 0.0 ± 0.0 | 0.1 ± 0.0 | 2.0 ± 0.1 | 0.0 ± 0.0 | 2.0 ± 0.1 | 169.1 ± 12.1 | **82.8 ± 7.2** | - | |
| Collias BAY | BDX21328 | Q | 6.00 | 0.0 ± 0.0 | 1.3 ± 0.1 | 1.0 ± 0.0 | 0.0 ± 0.0 | 0.0 ± 0.0 | 0.1 ± 0.0 | 2.4 ± 0.1 | 0.0 ± 0.0 | 2.4 ± 0.1 | 212.4 ± 12.0 | **87.1 ± 6.5** | - | |
| Collias BAY | BDX21329 | Q | 6.80 | 0.0 ± 0.0 | 1.4 ± 0.1 | 1.1 ± 0.1 | 0.0 ± 0.0 | 0.0 ± 0.0 | 0.1 ± 0.0 | 2.6 ± 0.1 | 0.0 ± 0.0 | 2.6 ± 0.1 | 202.5 ± 14.1 | **78.9 ± 6.7** | - | |
| Lautagne A FGQ | BDX18944 | FGQ | 0.73 | 0.3 ± 0.1 | 1.1 ± 0.1 | 0.7 ± 0.0 | 0.0 ± 0.0 | 0.0 ± 0.0 | 0.2 ± 0.0 | 2.3 ± 0.1 | 0.0 ± 0.0 | 2.3 ± 0.1 | 17.3 ± 0.4 | 7.5 ± 0.6 | - | |
| Lautagne A FGQ | BDX18945 | FGQ | 1.07 | 0.3 ± 0.1 | 1.2 ± 0.1 | 0.7 ± 0.0 | 0.0 ± 0.0 | 0.0 ± 0.0 | 0.2 ± 0.0 | 2.4 ± 0.1 | 0.0 ± 0.0 | 2.4 ± 0.1 | 42.5 ± 2.0 | 17.6 ± 1.5 | **16.0 - 20.8** | |
| Lautagne A FGQ | BDX18946 | FGQ | 1.47 | 0.3 ± 0.1 | 1.2 ± 0.1 | 0.8 ± 0.0 | 0.0 ± 0.0 | 0.0 ± 0.0 | 0.2 ± 0.0 | 2.5 ± 0.1 | 0.0 ± 0.0 | 2.5 ± 0.1 | 53.8 ± 2.0 | 21.8 ± 1.8 | **18.8 - 24.4** | |
| Lautagne A FGQ | BDX18947 | FGQ | 1.98 | 0.3 ± 0.1 | 1.2 ± 0.1 | 0.8 ± 0.0 | 0.0 ± 0.0 | 0.0 ± 0.0 | 0.2 ± 0.0 | 2.5 ± 0.1 | 0.0 ± 0.0 | 2.5 ± 0.1 | 63.0 ± 2.5 | 25.1 ± 2.1 | **20.9 - 27.2** | |
| Lautagne A FGQ | BDX18948 | FGQ | 2.35 | 0.4 ± 0.1 | 1.3 ± 0.1 | 0.8 ± 0.0 | 0.0 ± 0.0 | 0.0 ± 0.0 | 0.2 ± 0.0 | 2.7 ± 0.1 | 0.0 ± 0.0 | 2.7 ± 0.1 | 64.8 ± 1.8 | 24.3 ± 1.9 | **22.3 - 27.9** | |
| Lautagne A FGQ | BDX18949 | FGQ | 3.18 | 0.4 ± 0.1 | 1.4 ± 0.1 | 0.9 ± 0.0 | 0.0 ± 0.0 | 0.0 ± 0.0 | 0.1 ± 0.0 | 2.8 ± 0.1 | 0.0 ± 0.0 | 2.8 ± 0.1 | 80.8 ± 4.0 | 28.5 ± 2.5 | **24.7 - 31.4** | |
| Lautagne A FGQ | BDX18950 | FGQ | 3.53 | 0.3 ± 0.1 | 1.3 ± 0.1 | 0.9 ± 0.0 | 0.0 ± 0.0 | 0.0 ± 0.0 | 0.1 ± 0.0 | 2.7 ± 0.1 | 0.0 ± 0.0 | 2.7 ± 0.1 | 63.5 ± 2.6 | 23.3 ± 2.0 | **21.3 - 28.7** | |
| Lautagne A FGQ | BDX18953 | FGQ | 4.60 | 0.4 ± 0.1 | 1.5 ± 0.1 | 1.1 ± 0.1 | 0.0 ± 0.0 | 0.0 ± 0.0 | 0.1 ± 0.0 | 3.0 ± 0.1 | 0.0 ± 0.0 | 3.0 ± 0.1 | 93.4 ± 2.4 | 30.7 ± 2.4 | **27.9 - 34.3** | |

Q: coarse grain quartz; $\dot{D}_e$ values quotes as mean ± standard error of the mean.

BAY: coarse grain quartz (90-200 µm); $D_e$ representing the 'baSAR' central dose and the standard error of the central dose.

FGQ: fine grain grain quartz (4-11 µm); $D_e$ values quoted as mean ± standard error determined with the average dose model.

The final age calculations include the following systematic errors: $\dot{D}_\alpha$: 1 %, $\dot{D}_\beta$: 1 %, $\dot{D}_\gamma$: 5 % (in situ measurements ), $\dot{D}_\gamma$: 3 % ($\gamma$ -ray spectrometry ), β-source calibration: 3 %.

**Table 2**
AMS radiocarbon ages of samples from the sections Collias and Lautagne A (calibration by use of *IntCal13* according to Reimer et al., 2013)
Final ages used for this study are quoted in bold numbers.

| **Sample name** | **Laboratory code** | **Depth** (m) | **Material** (*species*) | **$^{14}$C age (a BP)** (1σ) | **Unmodeled $^{14}$C (a cal. BP)** (2σ) Min - Max | **Posterior calib. date (a b2k)** HPD (95%) From - To |
|---|---|---|---|---|---|---|
| Collias - 70/90 | DeA-21816 | 0.800 | shell (*P. muscorum*) | 11078 ± 49 | 12805 - 13067 | - |
| Collias - 90/100 | DeA-21817 | 0.950 | shell (*P. muscorum*) | 13683 ± 61 | 16268 - 16785 | - |
| Collias - 150/160 | DeA-21818 | 1.550 | shell (*P. muscorum*) | 23996 ± 123 | **27754 - 28369** | - |
| Collias - 220/230 | DeA-21819 | 2.250 | shell (*P. muscorum*) | 31515 ± 214 | **34894 - 35917** | - |
| Lautagne A - 50/60 | Ly-51291 | 0.550 | earthw. calcite granules | 8560 ± 35 | 9489 - 9554 | - |
| Lautagne A - 90/100 | DeA-18280 | 0.950 | shell (*P. muscorum*) | 14893 ± 64 | 17876 - 18355 | **17955 - 18347** |
| Lautagne A - 95/100 | GrA-68030 | 0.975 | earthw. calcite granules | 19250 ± 90 | 22918 - 23486 | - |
| Lautagne A - 140/150 | Ly-51292 | 1.450 | earthw. calcite granules | 9490 ± 40 | 10591 - 11069 | - |
| Lautagne A - 140/150 | DeA-18281 | 1.450 | shell (*P. muscorum*) | 10486 ± 48 | 12138 - 12575 | - |
| Lautagne A - 190/200 | Ly-51293 | 1.950 | earthw. calcite granules | 12530 ± 50 | 14420 - 15111 | - |
| Lautagne A - 200/210 | DeA-18282 | 2.050 | shell (*P. muscorum*) | 20527 ± 108 | 24358 - 25112 | **24410 - 25159** |
| Lautagne A - 240/250 | DeA-19359 | 2.450 | earthw. calcite granules | 18134 ± 73 | 21765 - 22253 | - |
| Lautagne A - 240/250 | DeA-19423 | 2.450 | earthw. calcite granules | 19929 ± 81 | 23722 - 24234 | - |
| Lautagne A - 250/260 | Ly-51294 | 2.550 | earthw. calcite granules | 17200 ± 70 | 20534 - 20969 | - |
| Lautagne A - 270/275 | GrA-68028 | 2.725 | earthw. calcite granules | 14790 ± 70 | 17791 - 18216 | - |
| Lautagne A - 280/290 | Ly-51295 | 2.850 | earthw. calcite granules | 14970 ± 60 | 17982 - 18372 | - |
| Lautagne A - 280/290 | GifA18096.1 | 2.850 | shell (*P. muscorum*) | 23260 ± 120 | 27302 - 27724 | **27334 - 27712** |
| Lautagne A - 280/290 | GifA18096.2 | 2.850 | shell (*P. muscorum*) | 23140 ± 130 | 27184 - 27667 | **27269 - 27678** |
| Lautagne A - 320/330 | GifA18097.1 | 3.250 | shell (*P. muscorum*) | 23040 ± 150 | 27068 - 27624 | **27228 - 27746** |
| Lautagne A - 320/330 | GifA18097.2 | 3.250 | shell (*P. muscorum*) | 24280 ± 150 | 27941 - 28670 | **27857 - 28563** |
| Lautagne A - 335/340 | GrA-68027 | 3.375 | earthw. calcite granules | 22040 ± 110 | 25989 - 26551 | - |
| Lautagne A - 380/390 | DeA-19360 | 3.850 | earthw. calcite granules | 19656 ± 80 | 23420 - 23949 | - |
| Lautagne A - 410/420 | GifA18098.1 | 4.150 | shell (*P. muscorum*) | 24110 ± 160 | 27800 - 28535 | **27905 - 28559** |
| Lautagne A - 410/420 | GifA18098.2 | 4.150 | shell (*P. muscorum*) | 23940 ± 160 | 27695 - 28381 | **27824 - 28484** |
| Lautagne A - 415/420 | GrA-68026 | 4.175 | earthw. calcite granules | 22400 ± 110 | 26329 - 27095 | - |
| Lautagne A - 440/450 | DeA-19361 | 4.450 | earthw. calcite granules | 21077 ± 90 | 25181 - 25659 | - |
| Lautagne A - 440/450 | DeA-19424 | 4.450 | earthw. calcite granules | 19561 ± 75 | 23287 - 23853 | - |

### *2.6.3. Bayesian age modelling*

In order to obtain a robust chronology of the best-dated sequence (Lautagne A), a Bayesian age model was built using the software *ChronoModel* (version 2.0.18) (Lanos and Dufresne, 2019; Lanos and Philippe, 2017, 2015). This software allows the calculation of *a posteriori* ages by considering the stratigraphic constraints between the samples. After removal of outliers, an age model was built for the period 35–15 ka cal. b2k (before the year 2000). We used the default configuration of Monte-Carlo Markov Chain (MCMC) parameters proposed by the software (3 chains, 1,000 burn iterations, and 500 batch iterations with a maximum of 20 batches, and 100,000 acquisition iterations with a thinning interval of 10). This approach may result in slightly underestimated age uncertainties because *ChronoModel* does not yet allow to specify shared systematic uncertainties. However, given the large uncertainties of the OSL ages, this potential problem does not affect the overall interpretation of our results.

In total, 15 $^{14}$C and OSL dates were used for establishing the chronology of the section Lautagne A (see **Fig. A5**). The highest posterior density (HPD, 95%) of the $^{14}$C and OSL ages was calculated according to the method detailed by Banks et al. (2019). The posterior age probability distributions for each sample are compiled in **Tables 1** and **2**.

## 3. Results

### 3.1. Lithofacies and soil horizons

*Homogeneous loess (Fm)*

This lithofacies consists of massive, homogeneous calcareous yellowish brown (10YR 5/4 to 2.5Y 6/4) coarse silt and fine sand (**Fig. 4A**). Bioturbation features (root channels, burrows) and secondary carbonate concretions (rhizoconcretions, pseudomycelium) are abundant (**Figs. 4, 5E, 5F, 6E** and **6F**). At Lautagne, a platy microstructure due to former segregation ice lenses (e.g., Van Vliet-Lanoë, 1985) is visible between 1.9 m and 3.2 m depth (**Fig. 6G**).

This lithofacies is dominant in both sections and interpreted as being of aeolian origin. Due to abundant secondary calcium carbonate, these loess units are designated as Ck or BCk horizons according to FAO (2006).

*Bedded calcareous sandy loess (Fh)*

This facies consists of regularly alternating sandy and light yellowish-brown silty (2.5Y 6/4) beds with lenses of small subangular limestone fragments (**Fig. 5B**). The lenses are ca 1 cm thick and generally up to 1 m wide (**Fig. 4B**). This lithofacies is interpreted as loess mixed with local coarser material, redistributed by overland flow.

*Massive loess colluvium (Dmm)*

Massive brown coarse silty deposits, containing scattered gravels, and characterised by poor sorting, greater porosity and few charcoal fragments, are interpreted as colluviated loess (**Figs. 2, 4B** and **5A**).

*Ploughed topsoil horizon (Ap)*

The topsoil horizon at Lautagne contains bricks, pottery and charcoal fragments and results from the reworking of loess caused by agricultural practices during the Holocene.

*Buried topsoil horizons with redox features (Ag)*

Five units in the section Lautagne A consist of thin (10–20 cm), slightly bleached (2.5Y 6/4 to 2.5Y 5/6), calcareous silt with scattered small Fe-Mn nodules. Their boundaries are sharp and show deformations due to stretching downslope (**Fig. 4E**). These horizons are characterised by (i) bleaching resulting from hydromorphic processes (iron reduction and removal from the horizon); (ii) a slightly finer texture compared to the underlying loess; (iii) weak staining by organic matter and (iv) abundant carbonate concretions.

These units, which often overlie BC horizons, are interpreted as topsoil Ag horizons, indicating seasonal waterlogging (FAO, 2006) that have been deformed by slope dynamics after burial, probably in a periglacial context, possibly by solifluction.

*Brown Bwk and BC horizons*

These horizons are characterised by moderate weathering as indicated by (i) a higher proportion of clay; (ii) a brown colour (10YR 5/6 to 10YR 6/6) related to the formation of iron oxides; (iii) partial dissolution of carbonates associated with carbonate precipitation in the underlying horizon. The Bwk horizon underwent strong secondary accumulation of calcite forming large rhyzoliths, which justifies the addition of the suffix –k. Poorly developed (incipient) horizons showing a range of features otherwise typical of Bw horizons are here referred to as BC horizons.

*Rubified Bw and Bwk horizons*

Yellowish red (5YR 4/6) to reddish brown (7.5YR 4/6), compact calcareous clayey silt units, exhibiting a massive or prismatic to blocky structure, are interpreted as rubified Bw horizons. Bioturbation (burrows and roots) is abundant, and black Fe-Mn hypocoatings cover many ped faces (**Fig. 6D**). There is no microscopic evidence of clay illuviation (e.g., clay coatings, clay papules) (**Fig. 5C**). Decalcification of the groundmass is complete, while some channels are filled by slightly calcareous loessic sediment. Secondary carbonate impregnations are also visible.

*Calcrete (Ckm horizon)*

At Collias, the redistribution of $CaCO_3$ led to the formation of an indurated laminar crust and vertical rhizoconcretions more than 10 cm long at the bottom of the profile, designated as Ckm horizon (**Fig. 4A, 4C**).

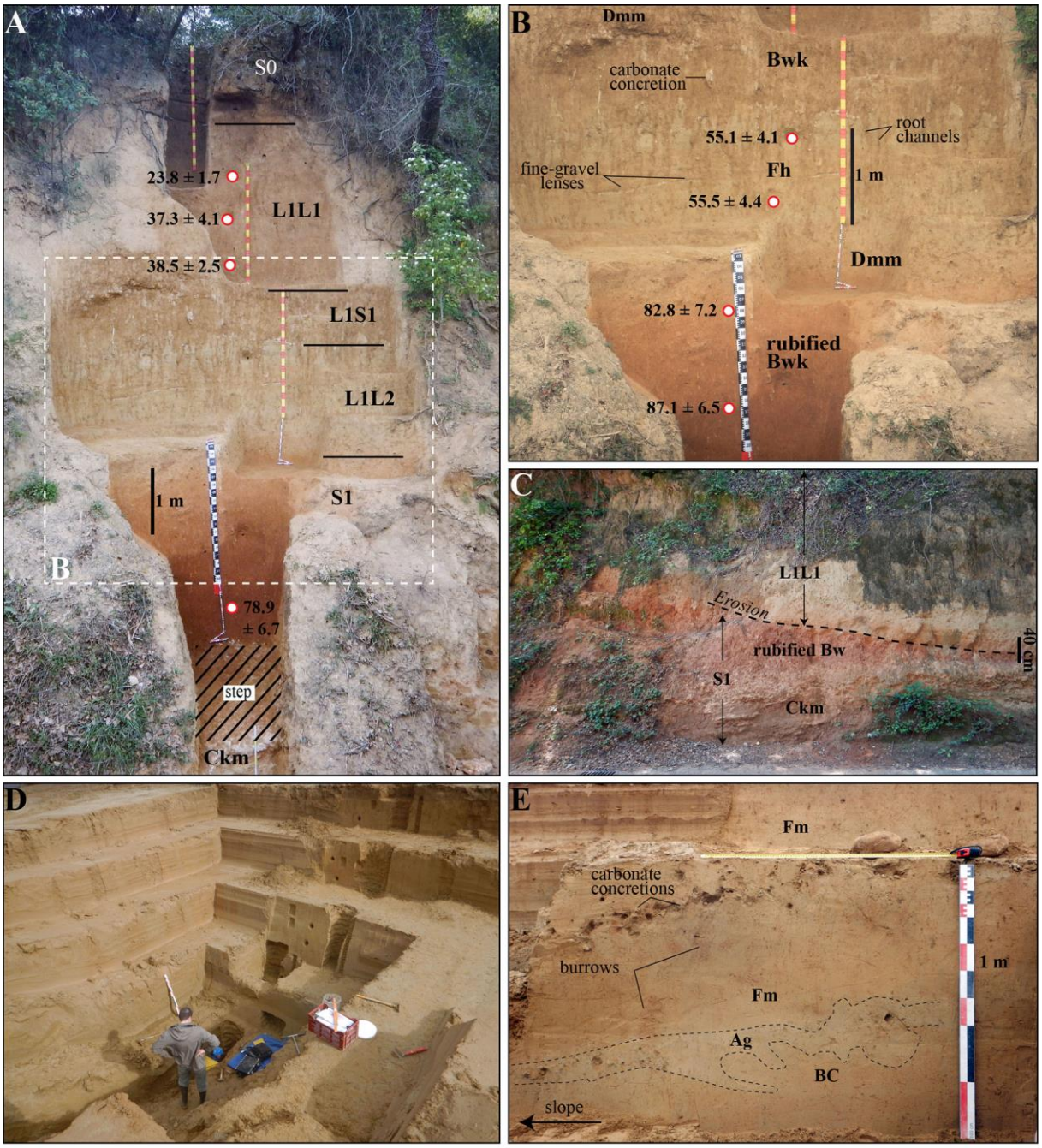


**Fig. 4**: A, B) Photographs of the main lithofacies of Collias with luminescence ages. C) Close-up view of the erosional surface above the rubified pedocomplex (S1) exposed in a roadcut approximately 100 m from the Collias section; D) Overview of the Lautagne section (Lautagne A) during archaeological excavations; E) Detail of the deformed incipient palaeosol (P2) of Lautagne (Lautagne B). All the photographs were taken by M. Bosq.

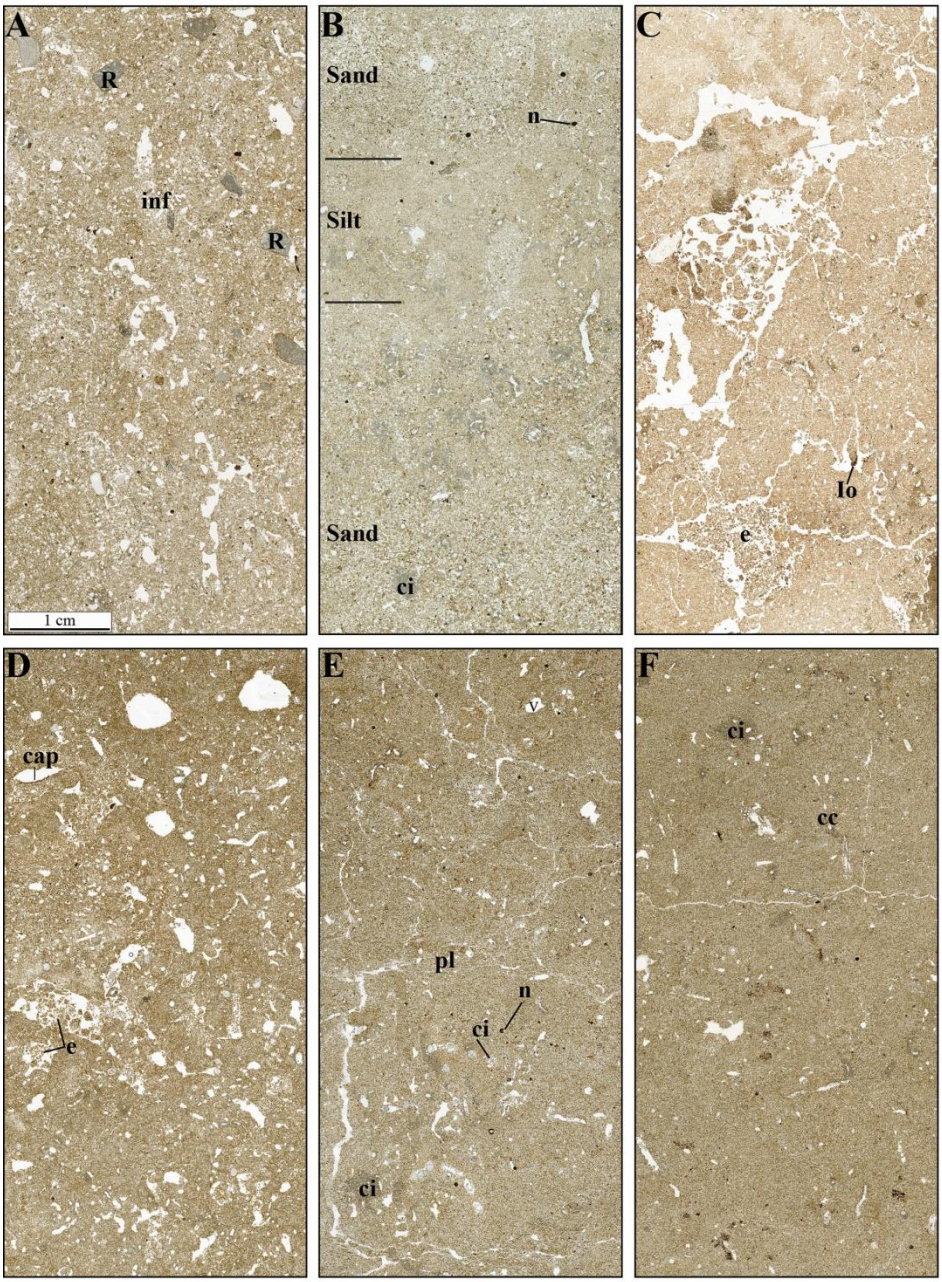


**Fig. 5**: Photographs of selected thin sections (6.5 cm x 3.0 cm) of the Collias (A, B and C) and Lautagne (D, E and F) sections. A) Brown Bwk horizon around 320 cm depth - channel microstructure with scattered rock fragments showing thin, clayey silt coatings (M3). B) Calcareous sandy loess (L1L2) around 400 cm depth – 3 cm to 5 cm thick beds of sand and silt, massive to channel microstructure with abundant secondary calcite impregnations; few scattered Fe/Mn nodules (M4). C) Rubified Bw horizon around 680 cm depth - subangular blocky macroaggregates (one to several centimetres in diameter) with completely decalcified reddish groundmass, diffuse Fe/Mn nodules and coatings. At the base of the thin section, loose discontinuous infillings with disintegrated excrements of enchytraeids or collembolas (M8). D) L1L1 loess near the top of the sequence - channel to vughy microstructure with complex packing voids and large abundant loose infillings of voids by disintegrated excrements (M8). E) Homogenous loess (L1L1) around 260 cm depth - poorly developed subangular blocky structure with carbonate impregnations. In places platy microstructure, partly destroyed by bioturbation (M4). F) Ag horizon around 280 cm depth - massive microstructure with weakly impregnated orthic Fe-hydroxyde nodules (M3). Abbreviations: cc=carbonate coating, ci=carbonate impregnation, cap=clayey silt capping, e=organo-mineral excrements, inf=infilling, Io=amorphous Fe-Mn hydroxides, n=Fe-Mn nodule, pl=platy microstructure R=rock fragment.

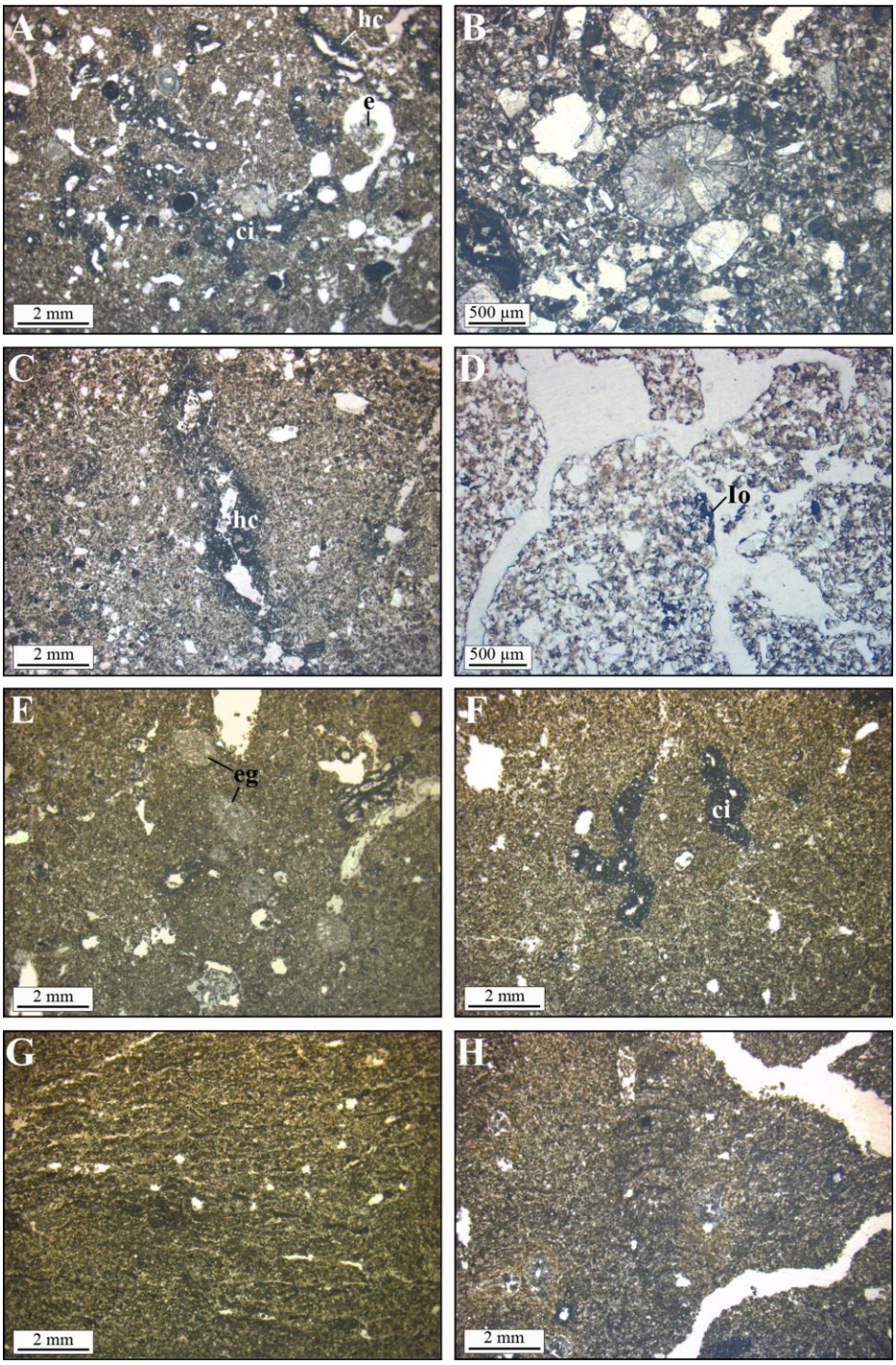


**Fig. 6**: Microfacies details of selected samples from Collias (A, B, C and D) and Lautagne A (E, F, G and H) sections (see **Figs. 2** and **3**) (plane-polarized (PPL)). A) L1L1 loess around 90 cm depth - dense incomplete micritic infillings and hypocoatings, and loose infilling of channels by porous organo-mineral microaggregates (M1). B) Brown Bwk horizon around 320 cm depth - earthworm granule showing radially arranged sparite crystals (M3). C) Calcareous sandy loess (L1L2) around 400 cm depth - calcite hypocoating around channel (M4). D) Rubified Bw horizon around 680 cm depth - Fe-Mn hypocoatings and quasicoatings (M8). E) L1L1 loess around 110 cm depth - earthworm granules (M7). F) Homogenous loess (L1L1) around 170 cm depth - calcitic impregnation (M6). G) Homogenous loess (L1L1) around 260 cm depth - platy microstructure (M4). H) Ag horizon around 280 cm depth - crescent fabric in silty groundmass, resulting from bioturbation by soil mesofauna (M3). Abbreviations: ci=carbonate impregnation, e=organo-mineral excrements, eg=earthworm granule, Hc=calcite hypocoating, Io=amorphous Fe-Mn hydroxides.

### 3.2. Stratigraphy

The section Collias comprises five main stratigraphic units, from bottom to top (**Figs. 2** and **4**):

- Calcrete (Ckm horizon) overlain by rubified Bw and Bwk horizons, forming a pedocomplex referred to as S1;
- Bedded calcareous sandy loess (L1L2), 2.5 m thick, with bioturbation and diffuse lower boundary;
- Brown Bwk horizon (L1S1), 0.5-0.6 m thick, whose upper boundary is an erosional surface;
- Colluvium (0.2 m) overlain by 2.8 m thick primary loess (L1L1);
- Holocene brown Cambisol (S0), about 1 m thick, predominantly composed of material that has been reworked and translocated in the course of agricultural land use and terracing of the above land (presently used as olive plantation).

The loess sequence at Lautagne (**Fig. 3**) covers Pleistocene gravels that were reached at a depth of 5.3 m during the archaeological excavation. Three main units (I-III) were distinguished:

- Reddish colluviated loess, up to 0.5 m thick (L1S1);
- Sandy, calcareous loess, 4.7 m thick (L1L1), including three incipient palaeosols (P3, P2 and P1), each consisting of an Ag-BC profile;
- Holocene Luvisol (S0), locally preserved from erosion due to agriculture within Gallo-Roman pits, and with a ploughed topsoil (Ap horizon).

### 3.3. Analytical data: magnetic susceptibility, colourimetry, grain-size and geochemistry

An overview of the main physical and chemical properties of the two sequences is provided in **Figures 2** and **3**.

Both sections are characterised by large GSI fluctuations with maximum values in the bedded loess at Collias (between 4.15 m and 4.50 m depth) and in the homogeneous (primary) loess at Lautagne A (at 3.15-3.30 m depth). The proportion of the coarse fraction (>100 µm) ranges from 6.3% to 34.8% at Collias and reflects slope material inputs mixed with aeolian dust and/or pedogenic carbonate concretions.

The variations in low-frequency magnetic susceptibility ($\chi_{LF}$) coincide with lithofacies changes in both sequences. The highest values ($\chi_{LF} \geq 0.4\ 10^{-6}$ $m^3/kg$) are found in palaeosol horizons while the lowest values are typical of primary loess (L1L1) and bedded loess (L1L2), except for the Bwk horizon L1S1 at Collias that has relatively low $\chi_{LF}$ values (between 0.25 and $0.39 \times 10^{-6}$ $m^3/kg$). L1S1 has also $\chi_{FD}$ values above 10%, indicating *in situ* neoformation of superparamagnetic (<0.03 µm) pedogenic particles. The lack of correlation between $\chi_{LF}$ and $\chi_{FD}$ values suggests that larger ferrimagnetic minerals (MD and SD) have little or no contribution to increased magnetic susceptibility.

A correlation exists between magnetic susceptibility and other proxies such as clay content and chromaticity a*. The highest values of chromaticity a* range between 5.6 and 13.5 and are associated with clay contents higher than 25%, especially in the pedocomplex S1 at Collias. At Lautagne A, the BC horizons are characterised by relatively high a* values (≥ 4), and an increase in clay content. In contrast, a* values and clay contents decrease in homogeneous loess (on average 8-14% clay at Lautagne A and 9-19% clay at Collias).

In both sequences, the element ratio Ti/Al is almost constant, with values between 0.07 and 0.09, indicating stable and homogeneous sediment sources. The Si/Al ratio covariates with CSI and increases significantly in loess while it decreases in palaeosol horizons, which reflects enrichment in aluminosilicates (clay minerals) in the latter. Plagioclase and K-feldspar weathering, represented by CPA and Rb/K, respectively, is more intense in B and BC horizons than in underlying loess. The weathering indices record maximum values in S1 with a CPA of about 96 and a Rb/K ratio of 63. Ag horizons exhibit higher concentrations of K-bearing minerals than BC horizons, which is related to the presence of illite in the fine fraction.

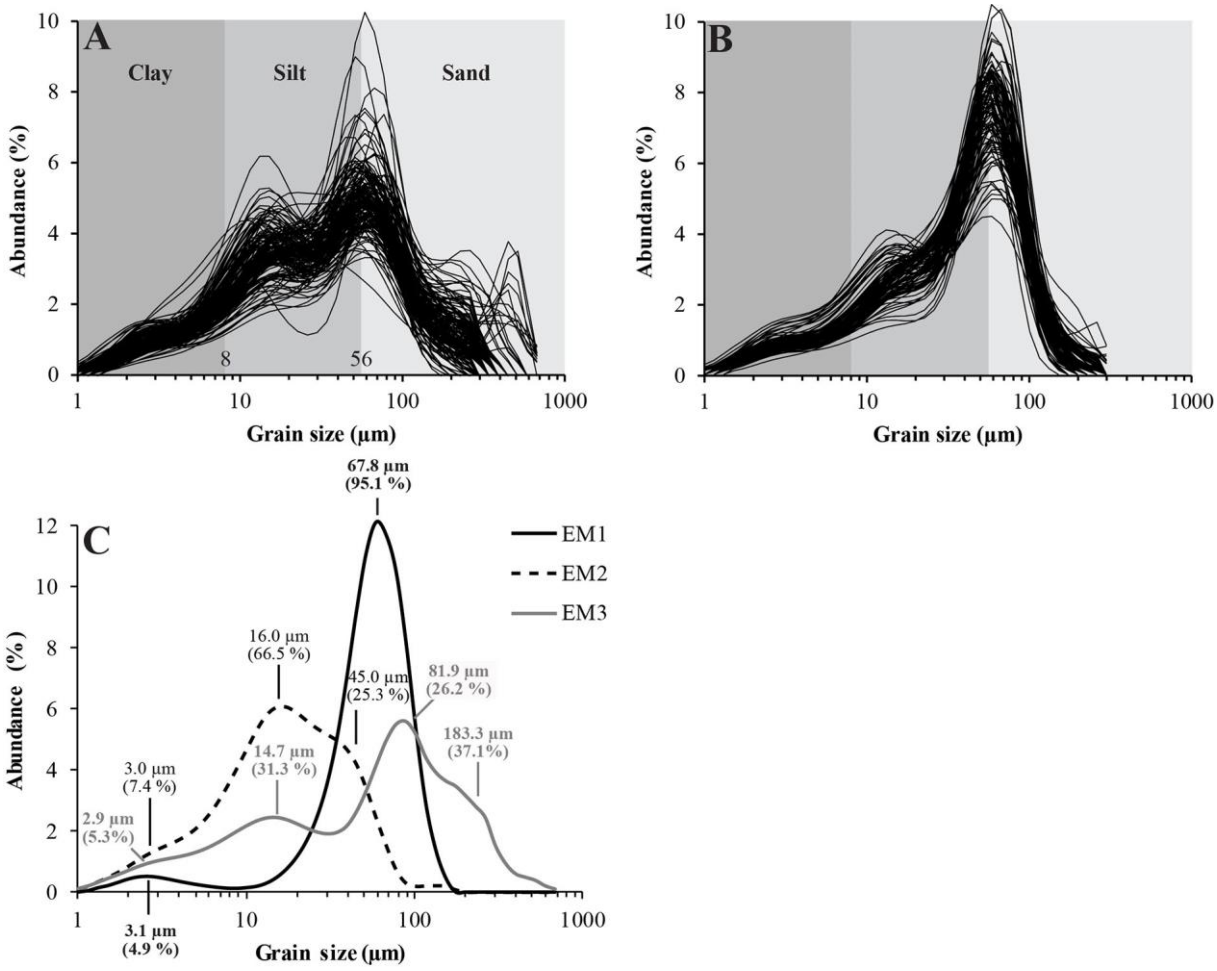


**Fig. 7**: Grain-size distribution of the samples from Collias (A) and Lautagne A (B). The upper limits of the grain-size classes used here are: 8 µm for clay and 56 µm for silt. C) End-member modelling results of the grain-size dataset of both sections. The main modes of the three end-members were determined by parametric curve-fitting using the R package 'mixdist' (Macdonald and Du, 2015).

### 3.4. Variation in Grain-size distribution and end-member modelling

The grain-size distribution of all samples is polymodal, with the main mode around 60–70 µm (**Figs. 7A, 7B**). The EM modelling algorithm is able to distinguish three components (EM-1, EM-2 and EM-3) that explain well the observed variability in grain-size distribution ($R^2$>0.9 for 95% of the samples analysed, i.e. 248 out of a total of 261).

EM-1 is characterised by a unimodal distribution with the main mode at 68 µm (**Fig. 7C**). This subpopulation explains 49.2% of the variance at Lautagne and 19.3% at Collias respectively. EM1 is interpreted as coarse particles that were transported by wind, through saltation and short-term suspension at very low altitude during storm events (Tsoar and Pye, 1987; Vandenberghe, 2013).

EM-2 has a roughly bimodal distribution with one mode in the medium silt fraction (45 µm) and another in fine silt (16 µm). It represents 40.3% of the variance at Collias and 33.0% at Lautagne A. The coarse mode (45 µm), common in loess deposits, involves short-term transport over greater distances than EM-1 (Li et al., 2018; Muhs and Bettis III, 2003; Pye, 1995). Recent observations in China showed that dust of the same grain-size mode (~40 µm) is collected 10 m above the ground during spring and early summer (Sun et al., 2003). The finest mode (16 µm) corresponds to dust transported through long-term suspension in the atmosphere at high altitude (tens to hundreds of metres above the ground (Sun et al., 2003). Observations in the Célé oasis (China) showed that these two components (45 µm and 16 µm) could derive from a single local source (Lin et al., 2016).

EM-3 is poorly sorted and has a polymodal distribution with the main mode of 183 µm and three minor modes (82 µm, 15 µm and 3 µm) (**Fig. 7C**). EM-3 explains 40.4% of the variance at Collias and 17.8% at Lautagne A. The presence of medium to coarse sand and poor sorting indicate mixing of materials from different sources (in surface horizons especially by agricultural practices) and the addition of autochthonous materials into the aeolian sediments by slope processes. EM-3 has probably a polygenic origin (aeolian and colluvial).

Fine grains (~3.0 µm mode) are represented by a tail in the grain-size distribution curves of all three subpopulations (**Fig. 7C**). This tail is sometimes considered as an artefact (Nottebaum et al., 2015), and is reported in most European and Asian loess deposits (Vandenberghe, 2013). The fine particles could indicate long-term suspension transport in the atmosphere ("continuous background dust") (Sun et al., 2002). Alternative hypotheses include: (i) fine particles transported by wind as aggregates (Újvári et al., 2016a); (ii) clay adhesion on coarser grains (Qiang et al., 2010) or (iii) pedogenic processes (Bronger and Heinkele, 1990; Sun et al., 2000).

Both sequences show the same overall pattern of EM distribution (**Fig. 8**), i.e. glacial loess deposits are dominated by the coarse component (mainly EM-1), whereas interglacial and interstadial palaeosol horizons are dominated by the fine component (EM-2). Topsoils and bedded loess that have undergone reworking are characterised by a higher EM-3 score.

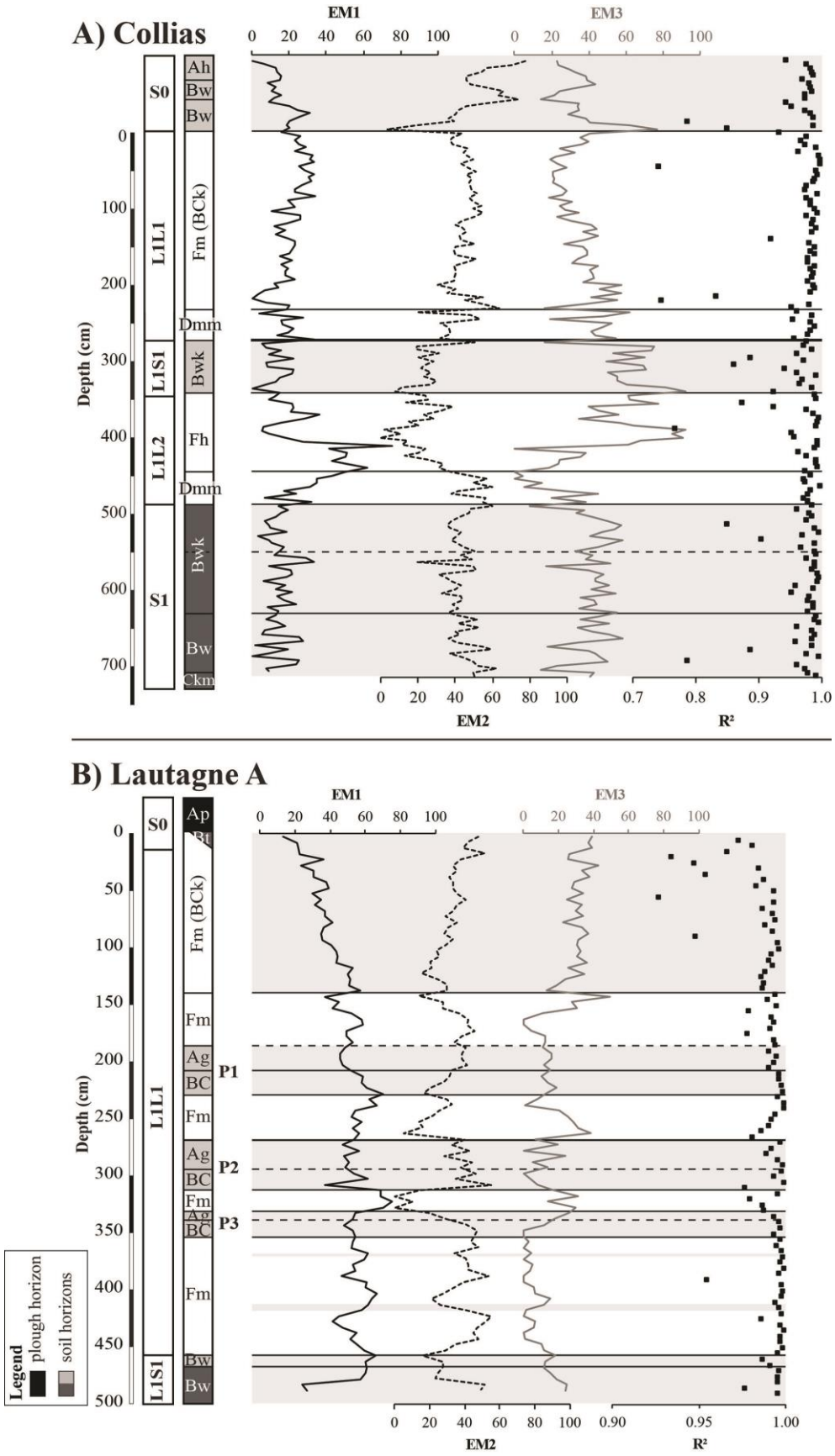


**Fig. 8**: Contribution of the three end-members and coefficient of determination ($R^2$) for each sample from the sections Collias (A) and Lautagne A (B).

### 3.5. Chronological data

#### 3.5.1. *Luminescence ages*

**Table 1** lists the luminescence ages in the two sections. Additional information is provided in **Appendix B**.

#### *3.5.2. Luminescence characteristics and equivalent doses*

All investigated quartz samples showed overall acceptable brightness and reproducibility (**Appendix B**). However, compared to the samples from Collias, the quartz fine grain (ca $10^6$ grains per aliquot) samples from Lautagne appeared rather dim, and additional tests on the coarse grain fraction (ca $10^2$ grains per aliquot) were not continued due to the low signal intensity.

Collias and Lautagne, showed broad $D_e$ distributions but without any obvious pattern. In the case of the samples from Collias this scatter may reflect poor bleaching, dose rate heterogeneities and/or sediment mixing. The presumed short transport distance from the Rhône Valley may not have yielded a full luminescence signal depletion. More likely, however, post-depositional mixing in conjunction with multiple short-distance erosion and deposition events occurred. Slope-wash and/or creep processes are evidenced by sand-sized and even fine- to medium-gravel sized particles, particularly in the L1L2 unit and the colluvial layer at the bottom of L1L1 at Collias (**Fig. 2**). Syn- and post-sedimentary bioturbation is also likely to have been involved.

For the samples from Lautagne (**Fig. B6**), the scatter is rather large for fine grain quartz samples with ca $10^6$ grains per aliquot and the expected averaging effects. However, the inter-aliquot scatter is dominated by the individual errors. Thus, these aliquots represent a common central dose.

#### *3.5.3. Dose rate results*

Th and K concentrations are comparable for the sites Collias and Lautagne (**Appendix B**). In both sites, the Th and K concentrations show a trend towards higher values in the lower Bw horizons (potential Th adsorption on clay particles). We found radioactive disequilibria in the U-decay chain at both sites. However, the onset of these disequilibria could not be determined, leading us to calculate an average value of the U concentration (see **Appendix B**).

#### *3.5.4. Luminescence ages results*

The OSL ages obtained for the loess deposits at Collias range from ~100 ka to ~25 ka. Age inversions overlap within uncertainties and are not considered significant. While the general pattern is similar for ages calculated as mean ± standard error of the mean (**Fig. B11**, displayed in blue) and those using the 'baSAR' modelling approach (**Fig. B11**, displayed in red), the Bayesian approach leads to significantly older ages in the lower part of the section. Nevertheless, given the luminescence ages and $D_e$ values close to commonly accepted

saturation values for quartz luminescence measured in the UV wavelength region, an age underestimation cannot be excluded, and the values must be interpreted cautiously.

The OSL ages obtained for the loess of the Lautagne A sequence range from 31.1 ± 2.4 ka to 7.5 ± 0.6 ka, and the ages are stratigraphically consistent within uncertainties (**Fig. B12**). **Figure 3** shows that the OSL estimates are consistent with the radiocarbon ages obtained from gastropod shells (see section 3.4.2). Only samples BDX18944 (7.5 ± 0.6 ka) and DeA-18281 (12.1–12.6 ka cal. BP) appear significantly underestimated and were not considered in the Bayesian age model. We assume that these young ages reflect an admixture of recent soil material through bioturbation.

### *3.5.5. Radiocarbon ages*

A total of 27 radiocarbon dates were determined from unit L1L1, including 23 at Lautagne A and 4 at Collias (**Table 2**).

At Lautagne A, the ages from *Pupilla muscorum* shells appear to be consistent with the stratigraphy and the OSL ages (**Fig. 9B**), while those from earthworm calcite granules show major stratigraphic inversions and younger ages (**Table 2**). The inconsistency of the latter can be explained by the following factors:

(i) lack of precise identification of the earthworm species that secreted these granules. Canti and Piearce (2003) show that some species (e.g., *Apporrectodea icteria*) deposit their granules at some depth, unlike other species (*Lumbricus terrestris* or *L. rubellus*) which preferentially release them on the soil surface. According to these authors, granules larger than 0.4 mm (i.e., the sieve mesh used in this study) can be produced only by a few earthworm species (mostly the genus *Lumbricus*). However, this statement needs to be confirmed as this study was based on current populations in the UK that are known to have smaller body sizes than those in more southerly latitudes, which acted as refuge areas during glacial period (Mathieu and Davies, 2014);

(ii) post-depositional movements resulting in granule redistribution along the soil profile. Earthworms commonly transport surface material (coarse sand, leaves, twigs) to the basal chamber of their burrows that can be located at up to 2 m depth (Canti, 2007). Syn-sedimentary bioturbation by roots may have been also involved.

Consequently, the ages from earthworm granules were excluded from the analysis to build the age-depth model of the sequence. However, only two dates (Ly-21291 and Ly-51292) among the 14 dates obtained from earthworm granules from the primary loess units yielded post-glacial ages. Thus, although the granules were not in a correct stratigraphic location, they provide reliable information on the age of loess deposition as a whole. Therefore, the ages obtained from Lautagne A (**Table 2**) and other loess sections (**Table 3**) were kept to calculate the age distribution of the Rhône Valley loess (see section **4.5.**).

### *3.5.6. Collias*

The sediment from the upper part of the S1 pedocomplex yielded ages (1σ) between ca 87.1 ± 6.5 ka and 82.8 ± 7.2 ka (Fig. 9A), suggesting that it was deposited during the Early Glacial. The lower loess (L1L2) was deposited between 82.8 ± 7.2 ka and 55.1 ± 4.4 ka, i.e. during the Lower Pleniglacial (~MIS 4-very beginning of MIS 3), and the upper loess (L1L1) between 38.5 ka and <23.8 ka, during the Upper Pleniglacial (late MIS 3-MIS 2). The Bwk horizon (L1S1) corresponds to the Middle Pleniglacial (~MIS 3). Discrepancies between $^{14}C$ and OSL ages at the top of L1L1 prevent an accurate estimation of the end of loess sedimentation.

### *3.5.7. Lautagne A*

According to a posteriori ages, the L1L1 loess of Lautagne A (4.60 m to 0.95 m depth) accumulated between ~31 ka b2k and 18 ka b2k (**Fig. 9B**), during the Greenland Stadials GS-5.2 to GS-2.1 (Rasmussen et al., 2014). This period was interspersed with the Greenland Interstadials GI-5.1 to GI-2.1, favourable for the genesis of palaeosols. As suggested by the age-depth model provided by ChronoModel, the incipient Ag-BC palaeosols within the L1L1 loess likely correlate with the interstadials. The 95.4% confidence interval of the a posteriori ages (27.6 – 27.2 ka b2k and 27.7 – 27.3 ka b2k) obtained for the most developed palaeosol P2 overlaps with the interstadial GI-3. With less certainty, P1 may be correlated to GI-2 and P3 to GI-4.

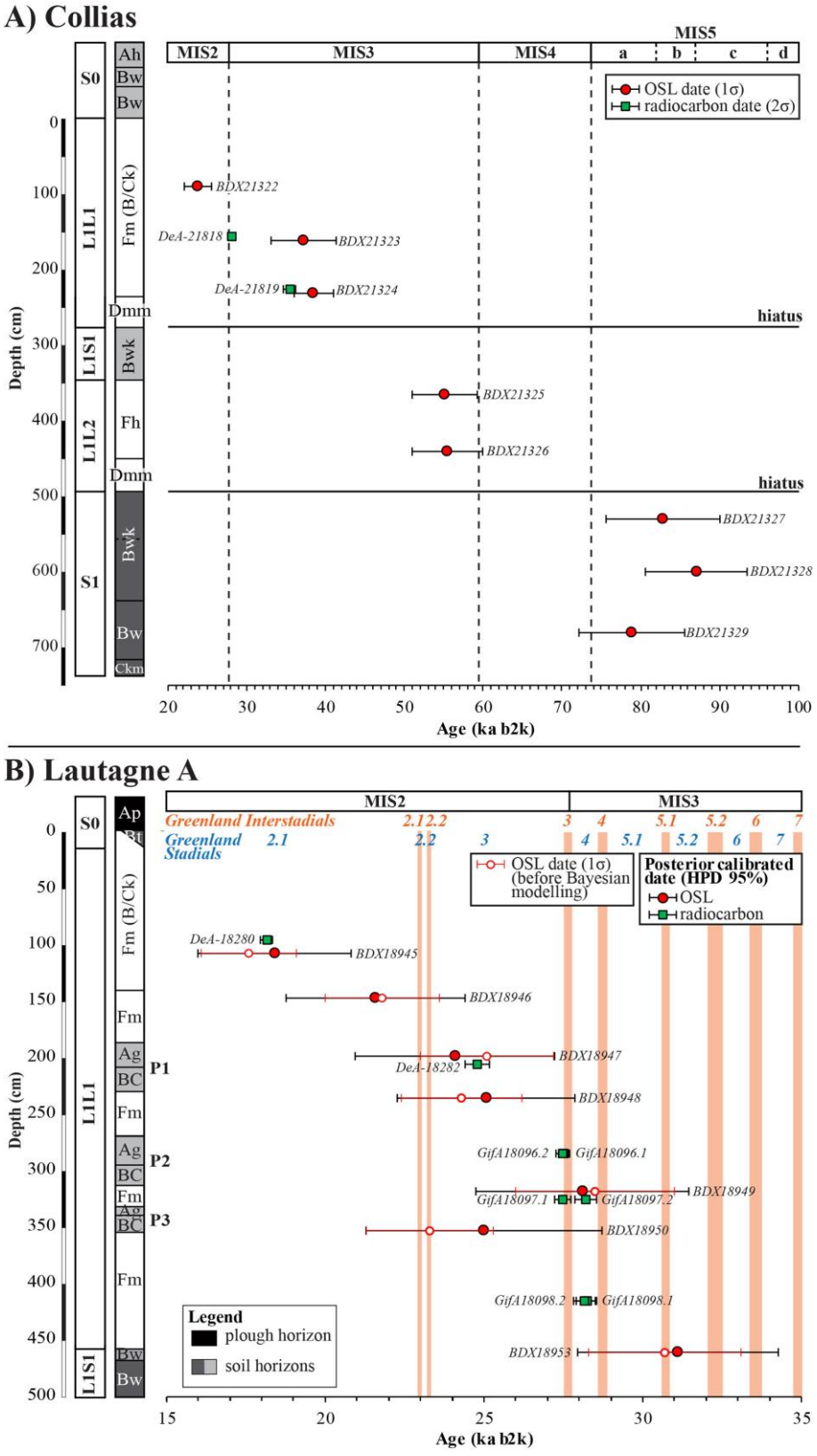


**Fig. 9**: Chronological data. A) Distribution of the OSL and radiocarbon ages of the section Collias obtained in this study. B) Posterior distribution (95%) of the ages for each sample derived from the Bayesian age model of the Lautagne section using *ChronoModel*. The OSL ages are generally consistent with the $^{14}C$ ages, although they have large error. Greenland interstadials from the NGRIP record on the GICC05 age model (Rasmussen et al., 2014) are indicated in orange.

# 4. Discussion

## 4.1. Eemian Interglacial and Early Glacial pedocomplex (S1)

The basal pedocomplex S1 at Collias is characterised by intense reddening, high clay content, chemical weathering, decalcification and precipitation of secondary carbonates in the underlying horizon, forming an indurated Ckm horizon (**Fig. 2**). Fe-Mn hypocoatings on the ped faces suggest occasional waterlogging (**Figs. 5C and 6D**). These characteristics are typical of red Mediterranean soils and testify a forest environment with strong seasonal moisture contrast leading to reddening (Durn et al., 2018; Fedoroff and Courty, 2013; Yaalon, 1997).

Considering the uncertainties associated with the OSL ages (82.8 ± 7.2 ka and 87.1 ± 6.5 ka), the material, in which the upper Bwk horizon of the pedocomplex formed, is attributed to the Early Glacial (MIS 5a-d). The underlying Bw and Ckm horizons can thus be correlated with the Last Interglacial (Eemian, MIS 5e) (**Figs. 2 and 9A**).

## 4.2. Lower Pleniglacial colluvium and bedded calcareous sandy loess (L1L2)

The Lower Pleniglacial started with the emplacement of loessic colluvium, comprising scattered gravel and reddish lenses containing charcoal fragments (**Fig. 3**). The colluvium reflects reworking of the red Interglacial/Early Glacial Bw horizons exposed along the slope.

Then, increased aridity and wind intensity led to the deposition of coarse-grained calcareous loess that has been redistributed and sorted by slopewash during rainstorm and/or snowmelt (**Figs. 3 and 8A**). The coarse texture indicates abundant sand transport from the sources, probably from the bed of the Rhône River (Bosq et al., 2020) since the particle size of the aeolian deposits becomes coarser towards this river (**Fig. 1B**). The presence of lenses of calcareous rock debris (**Fig. 4A, 4B**) indicates active frost weathering of limestone outcrops. Slope wash during rainstorms or snowmelt during summer are thought to be the main factor involved in the deposition of these lenses.

The OSL ages around 55 ka (BDX21325: 55.5 ± 4.4 ka and BDX21326: 55.1 ± 4.1 ka) suggest that loess deposition took place during late MIS 4 and/or the very beginning of MIS 3 (**Fig. 9A**). These periods are characterised by an increase in dust concentration in the Northern Hemisphere records, including the Greenland ice record (NGRIP; Ruth et al., 2003) and the Eifel Laminated Sediment Archive (ELSA) lake record in Germany (Seelos et al., 2009; Sirocko et al., 2016).

## 4.3. Middle Pleniglacial brown Bwk horizon (L1S1)

The brown Bwk horizon shows slight dissolution of carbonates, increased clay content and an increase in the concentration of pedogenic ultrafine magnetic grains. The lack of significant variation of weathering indices (CPA, Rb/K) indicates moderate silicate weathering (**Fig. 2**). Large rhizoliths formed below due to carbonate leaching and reprecipitation. The carbonate rhizoliths within the brown horizon must result from an interplay between pedogenesis and moderate loess accumulation rates. Thereby, the loess input led to an upward movement of

the soil surface and addition of primary carbonates, whereas pedogenesis involved leaching of these fresh inputs and accumulation of secondary carbonates within the lower part of the brown horizon (**Fig. 4B**). Thus, this brown Bwk horizon implies a decrease (possibly multiphased) in loess sedimentation and a moister climate favourable to the development of vegetation. The soil has been truncated by erosion and covered by colluvial material.

According to our chronological data, the soil to which the truncated Bwk horizon belonged formed between 55.1 ± 4.1 ka and 38.5 ± 2.5 ka (**Fig. 9A**), i.e. within a long interval during MIS 3.

### 4.4. Upper Pleniglacial loess (L1L1)

#### *4.4.1. Loess deposits*

The L1L1 loess reaches more than 2 m thickness at Collias and 4 m at Lautagne A (**Fig. 4**). Similar homogeneous yellowish, up to 5 m thick loess deposits were observed in many outcrops along the Rhône Valley (Bosq et al., 2018). They share common characteristics with the loess of the southern part of the Carpathian basin (e.g., Antoine et al., 2009b; Bokhorst et al., 2011; Marković et al., 2009; Novothny et al., 2011), including (i) coarse texture, (ii) lack of well-developed palaeosols; (iii) absence of structures of periglacial origin (ice-wedge pseudomorphs, soil wedges) except for platy microstructure; (iv) absence of laminated deposits of niveo-aeolian origin such as those commonly observed in NW Europe (Antoine et al., 2016; Lehmkuhl et al., 2016; Zens et al., 2018) and (v) abundant syn-sedimentary bioturbation.

The EM-1 subpopulation, which is predominant in the samples from Lautagne A (**Fig. 8B**), indicates a relatively limited transport distance, in the order of a few kilometres to tens of kilometres. This fraction originates from the Rhône riverbed, where the particles derived from the AIS were subjected to deflation. Riparian vegetation was probably involved in the trapping of wind-transported particles (e.g., Bosq et al., 2018).

The GSI peaks are interpreted as reflecting periods of increasing wind carrying capacity (Antoine et al., 2009a; Schirmer, 2016; Vandenberghe et al., 1985). According to the chronological data of Lautagne (**Fig. 9B**), the highest GSI values occurred during GS-3 and GS-4, whereas they slowly decreased during GS-2.1 (**Fig. 3**).

#### *4.4.2. Incipient palaeosols*

Weakly developed palaeosols (P1 to P3) are visible within the L1L1 loess at Lautagne A (**Fig. 3**). The Ag horizons are finer-grained than primary loess. They exhibit hydromorphic features and low organic matter content. The abundant carbonate concretions are interpreted as resulting from secondary carbonate precipitation during the accumulation of overlying loess, favoured by the fine- grained texture. The BC horizons have higher clay content, slight carbonate depletion and a slightly darker and reddish colour. Their genesis indicates short periods of decrease or cessation of loess sedimentation due to milder climate. The hydromorphic features in the topsoils can be explained by two hypotheses, which are not mutually exclusive:

(1) The soils developed during a period of climatic improvement associated with increased precipitation and snow accumulation. Waterlogging in the topsoil resulted from snow cover and subsequent snowmelt above still frozen ground that did not allow for meltwater infiltration. Permafrost was absent in the southern part of France during the coldest periods of the Pleistocene (Andrieux et al., 2016) and waterlogging occurred only during limited periods each year.

(2) Reducing conditions in the topsoil horizon occurred upon burial, as a consequence of soil organic matter degradation by soil microorganisms. Unlike the humic horizons described in the loess sections of continental Eastern Europe (e.g., Veres et al., 2018), soil-forming conditions in less continental regions led to the formation of poorly condensed organic matter with low "black carbon" content (Eckmeier et al., 2007; Schmidt and Noack, 2000), which was less resistant to degradation.

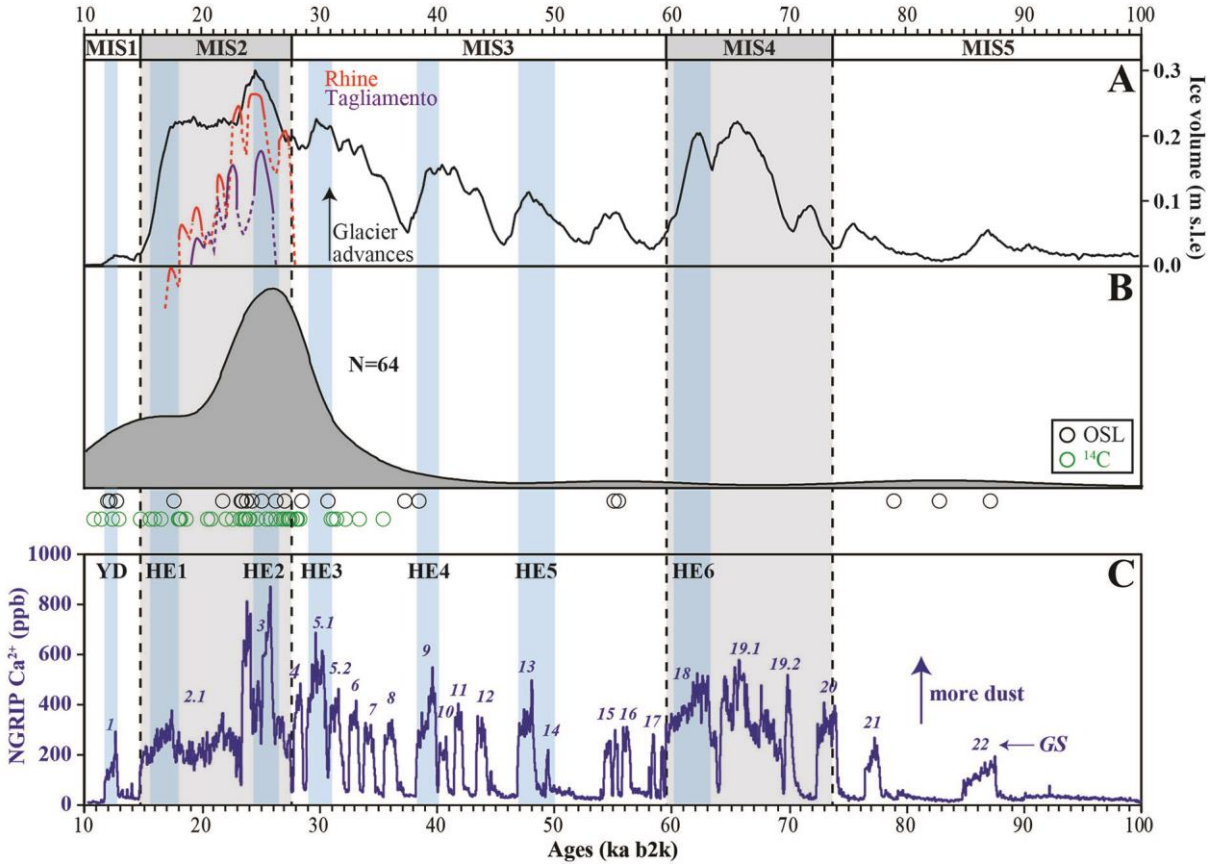


**Fig. 10**: A) Total AIS volume through the Last Glacial cycle (100–10 ka) from a recent simulation using the Parallel Ice Sheet Model (PISM) with climate forcing derived from WorldClim and the ERA-Interim reanalysis (Seguinot et al., 2018). Modelled ice volume is expressed in meters sea level equivalent (m s.l.e.). Fluctuations of the Rhine (red) (Preusser et al., 2011) and Tagliamento (purple) (Monegato et al., 2007) glaciers. B) Kernel Density Estimation (KDE) of ages for the OSL- and radiocarbon-dated loess from the Rhône Valley (this study, Ollivier, 2006; Bazile, 2007; Magnin, 2014; Varennes et al., 2015; Laroche et al., 2020; Thirault et al., 2020). C) NGRIP $Ca^{2+}$ curve over the last 100 ka according to the revised Greenland Ice Core Chronology (GICC05) proposed by Rasmussen et al. (2014). The chronological intervals for the Younger Dryas (YD) period and Heinrich Events (HEs) are depicted in blue. They are taken from Sanchez Goñi and Harrison (2010). The chronological limit of each MIS is also taken from Sanchez Goñi and Harrison (2010).

### 4.5. Regional chronology

In addition to the ages obtained in this study, we compiled the ages available for the loess deposits in southeast France from the literature to assess the chronology of the main regional sedimentation phases. Overall, 21 OSL dates on quartz and 43 $^{14}C$ dates on gastropod shells, earthworm granules and charcoal were selected (**Tables 1** to **4**). The age distribution was calculated using the Kernel Density Estimation (KDE) (Vermeesch, 2012), which helps to identify how ages cluster. The clusters provide a chronological estimate of the main periods of dust accumulation, assuming that sampling was equally distributed throughout the loess sequences. Although the analysis must be considered preliminary because of the limited number of available dates (N=64), the comparison of the KDE graph with the modelled AIS volume (expressed in metres of sea level equivalent) (Seguinot et al., 2018) together with the Rhine (Preusser et al., 2011) and the Tagliamento (Monegato et al., 2007) glacial systems for which robust chronological constraints are available on the one hand, and the dust concentration recorded in the NGRIP ice core ($Ca^{2+}$ in ppb) on the other hand, lead to the following conclusions (**Fig. 10**):

(1) For the period before ca 40 ka, only a few dates (N=5) are available, which suggests weak dust accumulation. Surprisingly, no age falls with certainty into MIS 4, a cold period that was marked by substantial AIS development. The reason behind remains unclear (weak deposition, subsequent erosion, loess recycling?).

(2) For the Upper Pleniglacial, the age distribution shows an approximate synchronicity between loess deposition and AIS fluctuations. The peak of loess ages at 28–24 ka, i.e. GS-3, coincides with the maximum AIS volume (26–23 ka, Ivy-Ochs et al., 2018; Luetscher et al., 2015; Monegato et al., 2017; Preusser et al., 2011; Seguinot et al., 2018) and the highest CSI values. This period includes Heinrich Event 2 (HE-2, Sanchez Goñi and Harrison, 2010), which was responsible for cold and arid conditions on the European continent (Duprat-Oualid et al., 2017; Fletcher et al., 2010).

(3) During the late Last Glacial Maximum (late LGM) (ca 23–19 ka, Clark et al., 2009), the AIS entered a recessional phase and lost 80% of its volume at 17.5 ka (Ivy-Ochs et al., 2008; Monegato et al., 2017). Following the deglaciation during GS-2, a significant glacial re-advance (not visible in the simulation) occurred during the Gschnitz stadial at 17–16 ka, in response to the HE-1 cooling (Ivy-Ochs et al., 2006, 2008; Ivy-Ochs, 2015). Accordingly, the age density decreases sharply during GS-2, while aeolian accumulation may have resumed somewhat during HE-1. Overall, GSI values gradually declined over this period.

(4) The aeolian activity persisted until the Younger Dryas cooling (GS-1) at 12.9–11.7 ka.

These preliminary results suggest that the peak of dust accumulation in the Rhône Valley was concomitant with the maximum AIS extension. The link between these two phenomena could reside in the modulation of the amount of glacially abraded fine particles by the advances and retreats of the ice sheet. These particles, which were transported by the Rhône River and its tributaries, and then remobilised by deflation, formed the main source of dust as shown by Bosq et al. (2020).

Therefore, glacier dynamics was probably the primary factor influencing loess deposition, whereas millennial climate fluctuations (HEs), including periods of enhanced dryness and associated changes in vegetation acted as a modulator of the primary signal.

**Table 3**

AMS radiocarbon ages of loess samples from other locations in the Rhône Valley (calibration by use of IntCal13 according to Reimer et al., 2013).

| Sample name | Laboratory code | Material | $^{14}$C a BP (1σ) | $^{14}$C a cal. BP (2σ) Min - Max | Reference |
|---|---|---|---|---|---|
| Lautagne B - 105/100 | GrA-68025 | earthw.calcite granules | 13250 ± 60 | 15722 - 16134 | this study |
| Lautagne B - 165/160 | GrA-68024 | earthw.calcite granules | 17000 ± 90 | 20221 - 20763 | this study |
| Lautagne B - 260/255 | GrA-68023 | earthw.calcite granules | 15340 ± 70 | 18440 - 18775 | this study |
| Mauves Sud 1 | Ly-14666 | earthw.calcite granules | 26870 ± 250 | 30651 - 31287 | this study |
| Mauves Sud 2 | Ly-14667 | earthw.calcite granules | 29370 ± 350 | 32698 - 34171 | this study |
| Saint-Paul-les-Durance 3 | Ly-14670 | earthw.calcite granules | 22880 ± 160 | 26776 - 27536 | this study |
| Saint-Paul-les-Durance 4 | Ly-14671 | earthw.calcite granules | 13030 ± 60 | 15324 - 15827 | this study |
| Collias 5 | Ly-14668 | earthw.calcite granules | 27540 ± 270 | 30976 - 31918 | this study |
| Saint-Désirat 2 | Ly-14669 | earthw.calcite granules | 21500 ± 140 | 25542 - 26043 | this study |
| Saint-Péray 3 | Ly-15407 | earthw.calcite granules | 19490 ± 100 | 23112 - 23784 | this study |
| Sathonay 1 | Ly-15408 | shell (*S. oblonga*) | 20020 ± 100 | 23809 - 24360 | this study |
| Sathonay 2 | Ly-15409 | shell (*S. oblonga*) | 22630 ± 140 | 26543 - 27316 | this study |
| Soyons 1 | Ly-15410 | shell (*S. oblonga*) | 18660 ± 90 | 22344 - 22769 | this study |
| Soyons 2 | Ly-15411 | shell (*S. oblonga*) | 27220 ± 230 | 30876 - 31456 | this study |
| Bouzil | Ly-390/AA-23353 | charcoal | 23570 ± 200 | 27390 - 28031 | Bazile, 2007 |
| Mirabeau 11 | Poz-17284 | charcoal | 11420 ± 140 | 13040 - 13547 | Ollivier, 2006 |
| Géménos-Aubagne | AA-16474 | charcoal | 32230 ± 490 | 35023 - 37596 | Magnin, 2014 |

**Table 4**

OSL ages of loess samples from other locations.

| Sample name | Laboratory code | Material | Age ka (1σ) | Reference |
|---|---|---|---|---|
| Les Croisières - UPS30 | GdTL-1878 | Quartz (125-200 µm) | 12.0 ± 0.5 | Varennes et al. (2015) |
| Les Croisières - UPS9 | GdTL-1877 | Quartz (125-200 µm) | 12.2 ± 0.8 | Varennes et al. (2015) |
| Garons ZAC Mitra V - PR116 | GdTL-2839 | Quartz (45-63 µm) | 27.0 ± 1.5 | Laroche et al. (2020) |
| Favary - PR1109 | GdTL-2190 | Quartz (45-63 µm) | 12.7 ± 0.7 | Thirault et al. (2020) |
| Lautagne B - OSL8 180cm | BDX18951 | Quartz (4-11 µm) | 26.3 ± 2.2 | This study |
| Lautagne B - OSL9 240cm | BDX18952 | Quartz (4-11 µm) | 23.4 ± 1.8 | This study |

## 5. Conclusions

The high-resolution multi-proxy sedimentological and chronostratigraphical analysis of two loess sections in the Rhône Valley allow to draw the following conclusions:

(1) A ~8 m thick loess record of the Last Climate Cycle is preserved at Collias. Loess deposition occurred during the Lower and Upper Pleniglacial (L1L2 and L1L1). The loess overlies a thick red pedocomplex (S1) developed during the Last Interglacial and the Early Glacial, similar to those observed elsewhere in southern and southeastern Europe (e.g., Durn et al., 2018; Fedoroff and Courty, 2013). A brown Bwk horizon

(L1S1) developed during the Middle Pleniglacial. In the Lautagne section, the ~ 5 m thick loess deposits provide a detailed record of the Upper Pleniglacial.

(2) The chronological data (AMS $^{14}C$ and OSL) show that the main phase of loess deposition (L1L1) corresponds to the stadials GS-5 to GS-2. The loess is coarse, calcareous and is interspersed with three incipient palaeosols at Lautagne A. These palaeosols are correlated with the Greenland Interstadials GI-4 to GI-2.

(3) At a regional scale, the numerical ages obtained on the upper loess (L1L1) range between ca 38.5 ka and 12 ka with a main peak at 28–24 ka, which coincides with the maximum AIS advance.

At a European scale, the aeolian systems composed of coversands and loess formed disconnected geographical units, each characterised by specific regional environmental conditions (i.e., regionally varying temperature, precipitation, and vegetation). It thus seems plausible that the phases of aeolian accumulation were not strictly synchronous across Europe, because the controlling factors (i.e., sediment availability, soil moisture, permafrost) varied considerably, both in time and space. This hypothesis remains, however, to be studied in more detail.

## Acknowledgements

This research was conducted in the PACEA laboratory with the financial support of the LaScArBx (research program of the Agence Nationale de la Recherche ANR-10-LABX-52), involving the University of Bordeaux and the University of Bordeaux-Montaigne. The preparation of the samples from Lautagne was greatly supported by the luminescence team from the Justus-Liebig University of Giessen (head: Prof Dr Markus Fuchs), namely Veit van Diedenhoven and Urs Tilmann Wolpert, who helped out in times of need. The preparation of the samples from Collias was made possible by the luminescence team from the University of Bayreuth (head: Dr Christoph Schmidt) who gave us access to their sieving equipment. The remaining sample preparation in Bordeaux was supported by Julie Faure and Pierre Bidaud. Additional support was also provided by the Institut national de recherches archéologiques Préventives (Inrap). C. Ronco and E. Morin who provided us an access to the archaeological excavations of Lautagne are warmly acknowledged. We also acknowledge the archaeologists who conducted the excavations and survey of Garons Mitra V, Soyons and Saint-Péray, particulary M. Laroche, J.-M. Lurol, B. Gely, J.-M. Le Pape, F. Derym. We would like to thank M. Rué, C. Recq, A. Ajas and J.-L. Brochier for providing us with their OSL dating results. We warmly thank Lee Drake for his invaluable help in calibration of the ED-XRF portable Bruker Tracer 5i. Finally, the two reviewers, F. Lehmkuhl and D.-D Rousseau are acknowledged for their valuable comments.

## References

[dataset] Amante, C., Eakins, B.W., 2009. ETOPO1 Global Relief Model converted to PanMap layer format. NOAA-National Geophysical Data Center. https://doi.org/10.1594/PANGAEA.769615

Andrieux, E., Bertran, P., Saito, K., 2016. Spatial analysis of the French Pleistocene permafrost by a GIS database. Permafrost and Periglacial Processes 27, 17–30.

Antoine, P., Rousseau, D.-D., Moine, O., Kunesch, S., Hatté, C., Lang, A., Tissoux, H., Zöller, L., 2009a. Rapid and cyclic aeolian deposition during the Last Glacial in European loess: a high-resolution record from Nussloch, Germany. Quaternary Science Reviews 28, 2955–2973. https://doi.org/10.1016/j.quascirev.2009.08.001

Antoine, P., Rousseau, D.-D., Fuchs, M., Hatté, C., Gauthier, C., Marković, S.B., Jovanović, M., Gaudenyi, T., Moine, O., Rossignol, J., 2009b. High-resolution record of the last climatic cycle in the southern Carpathian Basin (Surduk, Vojvodina, Serbia). Quaternary International 198, 19–36. https://doi.org/10.1016/j.quaint.2008.12.008

Antoine, P., Coutard, S., Guerin, G., Deschodt, L., Goval, E., Locht, J.-L., Paris, C., 2016. Upper Pleistocene loess-palaeosol records from Northern France in the European context: Environmental background and dating of the Middle Palaeolithic. Quaternary International 411, 4–24. https://doi.org/10.1016/j.quaint.2015.11.036

Bagnold, R.A., Barndorff-Nielsen, O., 1980. The pattern of natural size distributions. Sedimentology 27, 199–207. https://doi.org/10.1111/j.1365-3091.1980.tb01170.x

Banks, W.E., Bertran, P., Ducasse, S., Klaric, L., Lanos, P., Renard, C., Mesa, M., 2019. An application of hierarchical Bayesian modeling to better constrain the chronologies of Upper Paleolithic archaeological cultures in France between ca. 32,000–21,000 calibrated years before present. Quaternary Science Reviews 220, 188–214. https://doi.org/10.1016/j.quascirev.2019.07.025

Bazile, F., 2007. Le Gravettien de la France méditerranéenne. PALEO. Revue d'archéologie préhistorique 19, 89–103.

Bertran, P., Liard, M., Sitzia, L., Tissoux, H., 2016. A map of Pleistocene aeolian deposits in Western Europe, with special emphasis on France. Journal of Quaternary Science 31, e2909. https://doi.org/10.1002/jqs.2909

Boixadera, J., Poch, R.M., Lowick, S.E., Balasch, J.C., 2015. Loess and soils in the eastern Ebro Basin. Quaternary International 376, 114–133. https://doi.org/10.1016/j.quaint.2014.07.046

Bokhorst, M.P., Beets, C.J., Marković, S.B., Gerasimenko, N.P., Matviishina, Z.N., Frechen, M., 2009. Pedo-chemical climate proxies in Late Pleistocene Serbian–Ukranian loess sequences. Quaternary International 198, 113–123. https://doi.org/10.1016/j.quaint.2008.09.003

Bonifay, E., 1962. Les Terrains quaternaires dans le Sud-Est de la France. Delmas, Bordeaux.

Bosq, M., Bertran, P., Degeai, J.-P., Kreutzer, S., Queffelec, A., Moine, O., Morin, E., 2018. Last Glacial aeolian landforms and deposits in the Rhône Valley (SE France): Spatial distribution and grain-size characterization. Geomorphology 318, 250–269. https://doi.org/10.1016/j.geomorph.2018.06.010

Bosq, M., Bertran, P., Degeai, J.-P., Queffelec, A., Moine, O., 2020. Geochemical signature of sources, recycling and weathering in the Last Glacial loess from the Rhône Valley (southeast France) and comparison with other European regions. Aeolian Research 42, 100561. https://doi.org/10.1016/j.aeolia.2019.100561

Bouchez, J., Gaillardet, J., Lupker, M., Louvat, P., France-Lanord, C., Maurice, L., Armijos, E., Moquet, J.-S., 2012. Floodplains of large rivers: Weathering reactors or simple silos? Chemical Geology 332–333, 166–184. https://doi.org/10.1016/j.chemgeo.2012.09.032

Brennan, R., Quade, J., 1997. Reliable late-Pleistocene stratigraphic ages and shorter groundwater travel times from 14 C in fossil snails from the southern Great Basin. Quaternary Research 47, 329–336. https://doi.org/10.1006/qres.1997.1895

Bronger, A., Heinkele, Th., 1990. Mineralogical and clay mineralogical aspects of loess research. Quaternary International 7–8, 37–51. https://doi.org/10.1016/1040-6182(90)90037-5

Buggle, B., Glaser, B., Hambach, U., Gerasimenko, N., Marković, S., 2011. An evaluation of geochemical weathering indices in loess–paleosol studies. Quaternary International 240, 12–21. https://doi.org/10.1016/j.quaint.2010.07.019

Buggle, B., Hambach, U., Müller, K., Zöller, L., Marković, S.B., Glaser, B., 2014. Iron mineralogical proxies and Quaternary climate change in SE-European loess–paleosol sequences. Catena 117, 4–22. https://doi.org/10.1016/j.catena.2013.06.012

Calvo, F.R., Sánchez, J., Acosta, A., Wolf, D., Faust, D., 2016. Granulometrical, mineralogical and geochemical characterization of loess deposits in the Tajo Basin. Quaternary International 407, 14–28.

Canti, M.G., 2007. Deposition and taphonomy of earthworm granules in relation to their interpretative potential in Quaternary stratigraphy. Journal of Quaternary Science 22, 111–118. https://doi.org/10.1002/jqs.1017

Canti, M.G., Piearce, T.G., 2003. Morphology and dynamics of calcium carbonate granules produced by different earthworm species. Pedobiologia 47, 511–521. https://doi.org/10.1078/0031-4056-00221

CIE, 1976. Colorimetry: Official Recommendations of the International Commission on Illumination. Bureau central de la CIE, Paris.

Clark, P.U., Dyke, A.S., Shakun, J.D., Carlson, A.E., Clark, J., Wohlfarth, B., Mitrovica, J.X., Hostetler, S.W., McCabe, A.M., 2009. The Last Glacial Maximum. Science 325, 710–714. https://doi.org/10.1126/science.1172873

Combès, B., Philippe, A., Lanos, P., Mercier, N., Tribolo, C., Guerin, G., Guibert, P., Lahaye, C., 2015. A Bayesian central equivalent dose model for optically stimulated luminescence dating. Quaternary geochronology 28, 62–70. https://doi.org/10.1016/j.quageo.2015.04.001

Costantini, E.A.C., Carnicelli, S., Sauer, D., Priori, S., Andreetta, A., Kadereit, A., Lorenzettia, R., 2018. Loess in Italy: Genesis, characteristics and occurrence. Catena 168, 14-33. https://doi.org/10.1016/j.catena.2018.02.002

Cremaschi, M., 1990. The loess in Northern and Central Italy: a loess basin between the Alps and the Mediterranean Region, CNR Centro di Studio per la Stratigrafia e la Petrografia delle Alpi Centrali, Milano.

Cremaschi, M., Zerboni, A., Nicosia, C., Negrino, F., Rodnight, H., Spötl, C., 2015. Age, soil-forming processes, and archaeology of the loess deposits at the Apennine margin of the Po plain (northern Italy): New insights from the Ghiardo area. Quaternary International 376, 173–188. https://doi.org/10.1016/j.quaint.2014.07.044

Cullers, R.L., 2000. The geochemistry of shales, siltstones and sandstones of Pennsylvanian–Permian age, Colorado, USA: implications for provenance and metamorphic studies. Lithos 51, 181–203. https://doi.org/10.1016/S0024-4937(99)00063-8

Dearing, J., Livingstone, I., Zhou, L.-P., 1996. A late Quaternary magnetic record of Tunisian loess and its climatic significance. Geophysical Research Letters 23, 189–192. https://doi.org/10.1029/95GL03132

Dee, M.W., Palstra, S.W.L., Aerts-Bijma, A.T., Bleeker, M.O., de Bruijn, S., Ghebru, F., Jansen, H.G., Kuitems, M., Paul, D., Richie, R.R., 2020. Radiocarbon dating at Groningen: New and updated chemical pretreatment procedures. Radiocarbon 62, 63–74. https://doi.org/10.1017/RDC.2019.101

Dietze, E., Hartmann, K., Diekmann, B., IJmker, J., Lehmkuhl, F., Opitz, S., Stauch, G., Wünnemann, B., Borchers, A., 2012. An end-member algorithm for deciphering modern detrital processes from lake sediments of Lake Donggi Cona, NE Tibetan Plateau, China. Sedimentary Geology 243, 169–180. https://doi.org/10.1016/j.sedgeo.2011.09.014

Dietze, E., Dietze, M., 2019. Grain-size distribution unmixing using the R package EMMAgeo, E&G Quaternary Science Journal 68, 29–46. https://doi.org/10.5194/egqsj-68-29-2019

Drake, L., 2018. CloudCal v3.0. GitHub. https://github.com/leedrake5/CloudCal. doi:10.5281/zenodo.2596154

Duprat-Oualid, F., Rius, D., Bégeot, C., Magny, M., Millet, L., Wulf, S., Appelt, O., 2017. Vegetation response to abrupt climate changes in Western Europe from 45 to 14.7 k cal a BP: the Bergsee lacustrine record (Black Forest, Germany). Journal of Quaternary Science 32, 1008–1021. https://doi.org/10.1002/jqs.2972

Durcan, J.A., King, G.E., Duller, G.A., 2015. DRAC: Dose Rate and Age Calculator for trapped charge dating. Quaternary Geochronology 28, 54–61. https://doi.org/10.1016/j.quageo.2015.03.012

Durn, G., Wacha, L., Bartolin, M., Rolf, C., Frechen, M., Tsukamoto, S., Tadej, N., Husnjak, S., Li, Y., Rubinić, V., 2018. Provenance and formation of the red palaeosol and lithified terra rossa-like infillings on the Island of Susak: A high-resolution and chronological approach. Quaternary international 494, 105–129. https://doi.org/10.1016/j.quaint.2017.11.040

Eckmeier, E., Gerlach, R., Gehrt, E., Schmidt, M.W., 2007. Pedogenesis of chernozems in Central Europe—a review. Geoderma 139, 288–299. https://doi.org/10.1016/j.geoderma.2007.01.009

Ehlers, J., Gibbard, P.L., 2004. Quaternary glaciations-extent and chronology: part I: Europe. Elsevier, Amsterdam.

Evin, J., Marechal, J., Pachiaudi, C., Puissegur, Jj., 1980. Conditions involved in dating terrestrial shells. Radiocarbon 22, 545–555. https://doi.org/10.1017/S0033822200009875

FAO, 2006. Guideline for soil description, fourth ed. FAO, Rome, Italy.

Fedoroff, N., Courty, M.-A., 2013. Revisiting the genesis of red Mediterranean soils. Turkish Journal of Earth Sciences 22, 359–375. https://doi.org/10.3906/yer-1205-10

Fletcher, W.J., Goni, M.F.S., Allen, J.R., Cheddadi, R., Combourieu-Nebout, N., Huntley, B., Lawson, I., Londeix, L., Magri, D., Margari, V., 2010. Millennial-scale variability during the last glacial in vegetation records from Europe. Quaternary Science Reviews 29, 2839–2864. https://doi.org/10.1016/j.quascirev.2009.11.015

Frechen, M., Schirmer, W., 2011. Luminescence chronology of the Schwalbenberg II loess in the Middle Rhine valley. Eiszeitalter und Gegenwart 60, 78–89. https://doi.org/10.3285/eg.60.1.05

Fuchs, M., Kreutzer, S., Rousseau, D.-D., Antoine, P., Hatté, C., Lagroix, F., Moine, O., Gauthier, C., Svoboda, J., Lisá, L., 2013. The loess sequence of Dolní Vestonice, Czech Republic: A new OSL-based chronology of the Last Climatic Cycle. Boreas 42, 664–677. https://doi.org/10.1111/j.1502-3885.2012.00299.x

Goodfriend, G.A., Stipp, J.J., 1983. Limestone and the problem of radiocarbon dating of land-snail shell carbonate. Geology 11, 575–577. https://doi.org/10.1130/0091-7613(1983)11<575:LATPOR>2.0.CO;2

Guérin, Gilles, Antoine, P., Schmidt, E., Goval, E., Hérisson, D., Jamet, G., Reyss, J.-L., Shao, Q., Philippe, A., Vibet, M.-A., 2017. Chronology of the Upper Pleistocene loess sequence of Havrincourt (France) and associated Palaeolithic occupations: A Bayesian approach from pedostratigraphy, OSL, radiocarbon, TL and ESR/U-series data. Quaternary Geochronology 42, 15–30. https://doi.org/10.1016/j.quageo.2017.07.001

Guérin, Guillaume, Christophe, C., Philippe, A., Murray, A.S., Thomsen, K.J., Tribolo, C., Urbanova, P., Jain, M., Guibert, P., Mercier, N., Kreutzer, S., Lahaye, C., 2017. Absorbed dose, equivalent dose, measured dose rates, and implications for OSL age

estimates: Introducing the Average Dose Model. Quaternary Geochronology 41, 163–173. https://doi.org/10.1016/j.quageo.2017.04.002

Guibert, P., Schvoerer, M., 1991. TL dating: low background gamma spectrometry as a tool for the determination of the annual dose. International Journal of Radiation Applications and Instrumentation. Part D. Nuclear Tracks and Radiation Measurements 18, 231–238. https://doi.org/10.1016/1359-0189(91)90117-Z

Guilloré, P., 1980. Méthode de fabrication mécanique et en série des lames minces, Institut National Agronomique, Paris-Grignon.

Guo, Y., Yang, S., Su, N., Li, C., Yin, P., Wang, Z., 2018. Revisiting the effects of hydrodynamic sorting and sedimentary recycling on chemical weathering indices. Geochimica et Cosmochimica Acta 227, 48–63. https://doi.org/10.1016/j.gca.2018.02.015

Heier, K.S., Billings, G.K., 1970. Rubidium, in: Wedepohl K.H. (Eds.), Handbook of Geochemistry. Springer, Berlin, pp. 37B1-37N1.

Hopcroft, P.O., Valdes, P.J., Woodward, S., Joshi, M.M., 2015. Last glacial maximum radiative forcing from mineral dust aerosols in an Earth system model: LGM dust in an earth system model. Journal of Geophysical Research: Atmospheres 120, 8186–8205. https://doi.org/10.1002/2015JD023742

Hughes, A.L., Gyllencreutz, R., Lohne, Ø.S., Mangerud, J., Svendsen, J.I., 2016. The last Eurasian ice sheets–a chronological database and time-slice reconstruction, DATED-1. Boreas 45, 1–45.

Huntley, D.J., Godfrey-Smith, D.I., Thewalt, M.L., 1985. Optical dating of sediments. Nature 313, 105–107. https://doi.org/10.1038/313105a0

ISO, 2009. ISO 13320 - Particle size analysis - Laser diffraction methods.

IUSS Working Group WRB, 2015. World reference base for soil resources 2014, update 2015: International soil classification system for naming soils and creating legends for soil maps. FAO, Rome.

Ivy-Ochs, S., 2015. Glacier variations in the European Alps at the end of the last glaciation. Cuadernos de investigación geográfica 41, 295–315. https://doi.org/10.18172/cig.2750

Ivy-Ochs, S., Kerschner, H., Kubik, P.W., Schlüchter, C., 2006. Glacier response in the European Alps to Heinrich Event 1 cooling: the Gschnitz stadial. Journal of Quaternary science 21, 115–130. https://doi.org/10.1002/jqs.955

Ivy-Ochs, S., Kerschner, H., Reuther, A., Preusser, F., Heine, K., Maisch, M., Kubik, P.W., Schlüchter, C., 2008. Chronology of the last glacial cycle in the European Alps. Journal of Quaternary Science 23, 559–573. https://doi.org/10.1002/jqs.1202

Ivy-Ochs, S., Lucchesi, S., Baggio, P., Fioraso, G., Gianotti, F., Monegato, G., Graf, A.A., Akçar, N., Christl, M., Carraro, F., 2018. New geomorphological and chronological constraints for glacial deposits in the Rivoli-Avigliana end-moraine system and the lower Susa Valley (Western Alps, NW Italy). Journal of Quaternary Science 33, 550–562. https://doi.org/10.1002/jqs.3034

Ji, J., Balsam, W., Chen, J., 2001. Mineralogic and climatic interpretations of the Luochuan loess section (China) based on diffuse reflectance spectrophotometry. Quaternary Research 56, 23–30. https://doi.org/10.1006/qres.2001.2238

Jones, R.M., 2003. Particle size analysis by laser diffraction: ISO 13320, standard operating procedures, and Mie theory. American Laboratory 35, 44–47.

Kreutzer, S., Fuchs, M., Meszner, S., Faust, D., 2012a. OSL chronostratigraphy of a loess-palaeosol sequence in Saxony/Germany using quartz of different grain sizes. Quaternary Geochronology 10, 102–109. https://doi.org/10.1016/j.quageo.2012.01.004

Kreutzer, S., Schmidt, C., Fuchs, M.C., Dietze, M., Fischer, M., Fuchs, M., 2012b. Introducing an R package for luminescence dating analysis. Ancient TL 30, 1–8.

Kreutzer, S., Burow, C., Dietze, M., Fuchs, M.C., Schmidt, C., Fischer, M., Friedrich, J., Mercier, N., Smedley, R.K., Christophe, C., Zink, A., Durcan, J., King, G.E., Philippe, A., Guerin, G., Riedesel, S., Autzen, M., Guibert, P., Fuchs, M., 2020. Luminescence: Comprehensive Luminescence Dating Data Analysis. CRAN version 0.9.5. URL: https://CRAN.R-project.org/package=Luminescence.

Lambeck, K., Rouby, H., Purcell, A., Sun, Y., Sambridge, M., 2014. Sea level and global ice volumes from the Last Glacial Maximum to the Holocene. Proceedings of the National Academy of Sciences 111, 15296–15303. https://doi.org/10.1073/pnas.1411762111

Lanos, P., Dufresne, P., 2019. ChronoModel version 2.0: Software for Chronological Modelling of Archaeological Data Using Bayesian Statistics. Centre National de la Recherche Scientifique.

Lanos, P., Philippe, A., 2017. Event date model: a robust Bayesian tool for chronology building. Communications for Statistical Applications and Methods 25, 131–157. https://doi.org/10.29220/CSAM.2018.25.2.131

Lanos, P., Philippe, A., 2015. Hierarchical Bayesian modeling for combining dates in archaeological context. Journal de la Société Française de Statistique, Société Française de Statistique et Société Mathématique de France 158, 72–88.

Laroche, M., Parisot, N., Recq, C., Orgeval, M., Remicourt, M., Renaud, A., Grange, G., Charbouillot, S., Battentier, J., Marquebielle, B., Rué, M., Lafont, V., Chateauneuf, F., Curé, A.-M., Magnin, F., 2020. L'occupation fonbuxienne de Mitra 5 à Garons (Gard) (archaeological survey report). Paléotime, Villard-de-Lans.

Lehmkuhl, F., Zens, J., Krauß, L., Schulte, P., Kels, H., 2016. Loess-paleosol sequences at the northern European loess belt in Germany: Distribution, geomorphology and stratigraphy. Quaternary Science Reviews 153, 11–30. https://doi.org/10.1016/j.quascirev.2016.10.008

Li, Y., Song, Y., Fitzsimmons, K.E., Chang, H., Orozbaev, R., Li, X., 2018. Eolian dust dispersal patterns since the last glacial period in eastern Central Asia: insights from a loess-paleosol sequence in the Ili Basin. Climate of the Past 14, 271. https://doi.org/10.5194/cp-14-271-2018

Liang, L., Sun, Y., Beets, C.J., Prins, M.A., Wu, F., Vandenberghe, J., 2013. Impacts of grain size sorting and chemical weathering on the geochemistry of Jingyuan loess in the northwestern Chinese Loess Plateau. Journal of Asian Earth Sciences, New Global Perspectives on Paleontology, Stratigraphy, Paleoceanography, Paleoclimatology, and Tectonics in the East Asia and Western Pacific 69, 177–184. https://doi.org/10.1016/j.jseaes.2012.12.015

Lin, Y., Mu, G., Xu, L., Zhao, X., 2016. The origin of bimodal grain-size distribution for aeolian deposits. Aeolian Research 20, 80–88. https://doi.org/10.1016/j.aeolia.2015.12.001

Lindner, H., Lehmkuhl, F., Zeeden, C., 2017. Spatial loess distribution in the eastern Carpathian Basin: a novel approach based on geoscientific maps and data. Journal of Maps 13, 173–181. https://doi.org/10.1080/17445647.2017.1279083

Lomax, J., Fuchs, M., Preusser, F., Fiebig, M., 2014. Luminescence based loess chronostratigraphy of the Upper Palaeolithic site Krems-Wachtberg, Austria. Quaternary international 351, 88–97. https://doi.org/10.1016/j.quaint.2012.10.037

Løvborg, L., Kirkegaard, P., 1974. Response of 3 ″× 3 ″NaI (Tl) detectors to terrestrial gamma radiation. Nuclear Instruments and Methods 121, 239–251. https://doi.org/10.1016/0029-554X(74)90072-X

Lucas-Tooth, H.J., Price, B.J., 1961. A mathematical method for investigation of inter-element effects in X-ray fluorescent analysis. Metallurgia 64, 149–161.

Luetscher, M., Boch, R., Sodemann, H., Spötl, C., Cheng, H., Edwards, R.L., Frisia, S., Hof, F., Müller, W., 2015. North Atlantic storm track changes during the Last Glacial Maximum recorded by Alpine speleothems. Nature Communications 6, 1–6. https://doi.org/10.1038/ncomms7344

Lukić, T., Basarin, B., Buggle, B., Markovič, S.B., Tomović, V.M., Raljič, J.P., Hrnjak, I., Timar-Gabor, A., Hambach, U., Gavrilov, M.B., 2014. A joined rock magnetic and colorimetric perspective on the Late Pleistocene climate of Orlovat loess site (Northern Serbia). Quaternary International 334, 179–188. https://doi.org/10.1016/j.quaint.2014.03.042

Lunt, D.J., Valdes, P.J., 2002. Dust deposition and provenance at the Last Glacial Maximum and present day. Geophysical research letters 29, 42-1-42–4. https://doi.org/10.1029/2002GL015656

Macdonald, P., Du, J., 2015. Package 'mixdist': Finite Mixture Distribution Models. CRAN version 0.9.5. URL: https://CRAN.R-project.org/package=Luminescence.

Magnin, F., 2014. Middle Pleniglacial to Holocene molluscan assemblages in the Marseille-Aubagne basin (Provence, France). Quaternaire. Revue de l'Association française pour l'étude du Quaternaire 25, 113–125. https://doi.org/10.4000/quaternaire.7006

Maher, B.A., Taylor, R.M., 1988. Formation of ultrafine-grained magnetite in soils. Nature 336, 368–370. https://doi.org/10.1038/336368a0

Mahowald, N.M., Muhs, D.R., Levis, S., Rasch, P.J., Yoshioka, M., Zender, C.S., Luo, C., 2006. Change in atmospheric mineral aerosols in response to climate: Last glacial period, preindustrial, modern, and doubled carbon dioxide climates. Journal of Geophysical Research: Atmospheres 111, D10202 . https://doi.org/10.1029/2005JD006653

Mandier, P., 1988. Les problèmes chronologiques posés par les phases de la récession würmienne dans la moyenne vallée du Rhône. Quaternaire. Revue de l'Association française pour l'étude du Quaternaire 25, 123–128.

Marković, S.B., Hambach, U., Catto, N., Jovanović, M., Buggle, B., Machalett, B., Zöller, L., Glaser, B., Frechen, M., 2009. Middle and late Pleistocene loess sequences at Batajnica, Vojvodina, Serbia. Quaternary International 198, 255–266. https://doi.org/10.1016/j.quaint.2008.12.004

Mathieu, J., Davies, T.J., 2014. Glaciation as an historical filter of below-ground biodiversity. Journal of Biogeography 41, 1204–1214. https://doi.org/10.1111/jbi.12284

Mazenot, G., 1956. Recherches sur les faunes malacologiques du loess récent würmien et de divers limons terrestres holocènes dans le sud-est de la France. Bulletin mensuel de la Société linnéenne de Lyon 25, 9–24.

Mercier, N., Falguères, C., 2007. Field gamma dose-rate measurement with a NaI (Tl) detector: re-evaluation of the "threshold" technique. Ancient TL 25, 1–4.

Mercier, N., Kreutzer, S., Christophe, C., Guérin, G., Guibert, P., Lahaye, C., Lanos, P., Philippe, A., Tribolo, C., 2016. Bayesian statistics in luminescence dating: The'baSAR'-model and its implementation in the R package'Luminescence'. Ancient TL 34, 14–21.

Miall, A., 1996. The Geology of Fluvial Deposits, Sedimentary Facies, Basin Analysis and Petroleum Geology. Springer, Berlin.

Moine, O., Antoine, P., Hatté, C., Landais, A., Mathieu, J., Prud'homme, C., Rousseau, D.-D., 2017. The impact of Last Glacial climate variability in west-European loess revealed by radiocarbon dating of fossil earthworm granules. Proceedings of the

National Academy of Sciences 114, 6209–6214. https://doi.org/10.1073/pnas.1614751114
Molnár, M., Rinyu, L., Veres, M., Seiler, M., Wacker, L., Synal, H.-A., 2013. EnvironMICADAS: A mini 14 C AMS with enhanced gas ion source interface in the Hertelendi Laboratory of Environmental Studies (HEKAL), Hungary. Radiocarbon 55, 338–344. https://doi.org/10.1017/S0033822200057453
Monegato, G., Ravazzi, C., Donegana, M., Pini, R., Calderoni, G., Wick, L., 2007. Evidence of a two-fold glacial advance during the last glacial maximum in the Tagliamento end moraine system (eastern Alps). Quaternary Research 68, 284–302. https://doi.org/10.1016/j.yqres.2007.07.002
Monegato, G., Scardia, G., Hajdas, I., Rizzini, F., Piccin, A., 2017. The Alpine LGM in the boreal ice-sheets game. Scientific reports 7, 1–8. https://doi.org/10.1038/s41598-017-02148-7
Moska, P., Jary, Z., Adamiec, G., Bluszcz, A., 2019. Chronostratigraphy of a loess-palaeosol sequence in Biały Kościół, Poland using OSL and radiocarbon dating. Quaternary international 502, 4–17. https://doi.org/10.1016/j.quaint.2018.05.024
Moska, P., Jary, Z., Adamiec, G., Bluszcz, A., 2015. OSL chronostratigraphy of a loess-palaeosol sequence in Złota using quartz and polymineral fine grains. Radiation Measurements 81, 23–31. https://doi.org/10.1016/j.radmeas.2015.04.012
Muhs, D.R., Bettis III, E.A., 2003. Quaternary loess-paleosol sequences as examples of climate-driven sedimentary extremes. Special Papers-Geological Society of America 370, 53–74.
Munsell, A.H., 2000. Munsell soil color charts. GretagMacbeth, Shanghai.
Murray, A.S., Wintle, A.G., 2000. Luminescence dating of quartz using an improved single-aliquot regenerative-dose protocol. Radiation measurements 32, 57–73. https://doi.org/10.1016/S1350-4487(99)00253-X
Nesbitt, H.W., Markovics, G., Price, R.C., 1980. Chemical processes affecting alkalis and alkaline earths during continental weathering. Geochimica et Cosmochimica Acta 44, 1659–1666. https://doi.org/10.1016/0016-7037(80)90218-5
Nesbitt, H.W., Young, G.M., 1989. Formation and Diagenesis of Weathering Profiles. The Journal of Geology 97, 129–147. https://doi.org/10.1086/629290
Nesbitt, H.W., Young, G.M., 1982. Early Proterozoic climates and plate motions inferred from major element chemistry of lutites. Nature 299, 715. https://doi.org/10.1038/299715a0
Nottebaum, V., Stauch, G., Hartmann, K., Zhang, J., Lehmkuhl, F., 2015. Unmixed loess grain size populations along the northern Qilian Shan (China): relationships between geomorphologic, sedimentologic and climatic controls. Quaternary International 372, 151–166. https://doi.org/10.1016/S1350-4487(99)00253-X
Novothny, Á., Frechen, M., Horváth, E., Wacha, L., Rolf, C., 2011. Investigating the penultimate and last glacial cycles of the Süttő loess section (Hungary) using luminescence dating, high-resolution grain size, and magnetic susceptibility data. Quaternary International 234, 75–85. https://doi.org/10.1016/j.quaint.2010.08.002
Obreht, I., Zeeden, C., Hambach, U., Veres, D., Marković, S.B., Lehmkuhl, F., 2019. A critical reevaluation of palaeoclimate proxy records from loess in the Carpathian Basin. Earth-science reviews 190, 498-520. https://doi.org/10.1016/j.earscirev.2019.01.020
Ollivier, V., 2006. Continuités, instabilités et ruptures morphogéniques en Provence depuis la dernière glaciation. Travertinisation, détritisme et incisions sur le piémont sud du Grand Luberon (Vaucluse, France). Relations avec les changements climatiques et

l'anthropisation (Unpublished Ph.D. dissertation). University of Provence, Aix-Marseille I.

Paterson, G.A., Heslop, D., 2015. New methods for unmixing sediment grain size data. Geochemistry, Geophysics, Geosystems 16, 4494–4506. https://doi.org/10.1002/2015GC006070

Pigati, J.S., Rech, J.A., Nekola, J.C., 2010. Radiocarbon dating of small terrestrial gastropod shells in North America. Quaternary Geochronology 5, 519–532. https://doi.org/10.1016/j.quageo.2010.01.001

Preusser, F., Degering, D., Fuchs, M., Hilgers, A., Kadereit, A., Klasen, N., Krbetschek, M., Richter, D., Spencer, J.Q., 2008. Luminescence dating: basics, methods and applications. E&G Quaternary Science Journal 57, 95–149.

Preusser, F., Graf, H.R., Keller, O., Krayss, E., Schlüchter, C., 2011. Quaternary glaciation history of northern Switzerland. E&G Quaternary Science Journal 60, 282–305. https://doi.org/10.3285/eg.60.2-3.06

Profe, J., Zolitschka, B., Schirmer, W., Frechen, M., Ohlendorf, C., 2016. Geochemistry unravels MIS 3/2 paleoenvironmental dynamics at the loess–paleosol sequence Schwalbenberg II, Germany. Palaeogeography, Palaeoclimatology, Palaeoecology 459, 537–551. https://doi.org/10.1016/j.palaeo.2016.07.022

Pye, K., 1995. The nature, origin and accumulation of loess. Quaternary Science Reviews 14, 653–667. https://doi.org/10.1016/0277-3791(95)00047-X.

Qiang, M., Lang, L., Wang, Z., 2010. Do fine-grained components of loess indicate westerlies: insights from observations of dust storm deposits at Lenghu (Qaidam Basin, China). Journal of Arid Environments 74, 1232–1239. https://doi.org/10.1016/j.jaridenv.2010.06.002

Qin, X., Cai, B., Liu, T., 2005. Loess record of the aerodynamic environment in the east Asia monsoon area since 60,000 years before present. Journal of Geophysical Research: Solid Earth 110, B01204.https://doi.org/10.1029/2004JB003131.

R Core Team, 2019. R: a language and environment for statistical computing, version 3.0. 2. Vienna, Austria: R Foundation for Statistical Computing; 2013.

Rasmussen, S.O., Bigler, M., Blockley, S.P., Blunier, T., Buchardt, S.L., Clausen, H.B., Cvijanovic, I., Dahl-Jensen, D., Johnsen, S.J., Fischer, H., 2014. A stratigraphic framework for abrupt climatic changes during the Last Glacial period based on three synchronized Greenland ice-core records: refining and extending the INTIMATE event stratigraphy. Quaternary Science Reviews 106, 14–28. https://doi.org/10.1016/j.quascirev.2014.09.007

Reimann, C., Birke, M., Demetriades, A., Filzmoser, P., O'Connor, P., 2014. Part A: Chemistry of Europe's Agricultural Soils: Methodology and Interpretation of the GEMAS Data Set. Geologisches Jahrbuch, Hannover.

Reimer, P.J., Bard, E., Bayliss, A., Beck, J.W., Blackwell, P.G., Ramsey, C.B., Buck, C.E., Cheng, H., Edwards, R.L., Friedrich, M., 2013. IntCal13 and Marine13 radiocarbon age calibration curves 0–50,000 years cal BP. Radiocarbon 55, 1869–1887. https://doi.org/10.2458/azu_js_rc.55.16947

Richter, D., Richter, A., Dornich, K., 2013. Lexsyg—A new system for luminescence research. Geochronometria 40, 220–228. https://doi.org/10.2478/s13386-013-0110-0

Ruth, U., Wagenbach, D., Steffensen, J.P., Bigler, M., 2003. Continuous record of microparticle concentration and size distribution in the central Greenland NGRIP ice core during the last glacial period. Journal of Geophysical Research: Atmospheres 108. https://doi.org/10.1029/2002JD002376

Sanchez Goñi, M.F., Harrison, S.P., 2010. Millennial-scale climate variability and vegetation changes during the Last Glacial: Concepts and terminology. Quaternary Science Reviews 29, 2823–2827. https://doi.org/10.1016/j.quascirev.2009.11.014

Sauer, D., Kadereit, A., Kühn, P., Kösel, M., Miller, C.E., Shinonaga, T., Kreutzer, S., Herrmann, L., Fleck, W., Starkovich, B.M., Stahr, K., 2016. The loess-palaeosol sequence of Datthausen, SW Germany: Characteristics, chronology, and implications for the use of the Lohne Soil as a marker soil. Catena 146, 10–29. https://doi.org/10.1016/j.catena.2016.06.024

Schaffernicht, E.J., Ludwig, P., Shao, Y., 2020. Linkage between dust cycle and loess of the Last Glacial Maximum in Europe. Atmospheric Chemistry and Physics 20, 4969–4986. https://doi.org/10.5194/acp-20-4969-2020

Schirmer, W., 2016. Late Pleistocene loess of the lower Rhine. Quaternary international 411, 44–61. https://doi.org/10.1016/j.quaint.2016.01.034

Schmidt, M.W., Noack, A.G., 2000. Black carbon in soils and sediments: analysis, distribution, implications, and current challenges. Global biogeochemical cycles 14, 777-793. https://doi.org/10.1029/1999GB001208

Schulte, P., Lehmkuhl, F., Steininger, F., Loibl, D., Lockot, G., Protze, J., Fischer, P., Stauch, G., 2016. Influence of HCl pretreatment and organo-mineral complexes on laser diffraction measurement of loess–paleosol sequences. Catena 137, 392–405. https://doi.org/10.1016/j.catena.2015.10.015

Seelos, K., Sirocko, F., Dietrich, S., 2009. A continuous high-resolution dust record for the reconstruction of wind systems in central Europe (Eifel, Western Germany) over the past 133 ka. Geophysical Research Letters 36, L20712. https://doi.org/10.1029/2009GL039716

Seguinot, J., Ivy-Ochs, S., Jouvet, G., Huss, M., Funk, M., Preusser, F., 2018. Modelling last glacial cycle ice dynamics in the Alps. The Cryosphere 12, 3265–3285. https://doi.org/10.3929/ethz-b-000297918

Sheldon, N.D., Tabor, N.J., 2009. Quantitative paleoenvironmental and paleoclimatic reconstruction using paleosols. Earth-Science Reviews 95, 1–52. https://doi.org/10.1016/j.earscirev.2009.03.004

Sirocko, F., Knapp, H., Dreher, F., Förster, M.W., Albert, J., Brunck, H., Veres, D., Dietrich, S., Zech, M., Hambach, U., Röhner, M., Rudert, S., Schwibus, K., Adams, C., Sigl, P., 2016. The ELSA-Vegetation-Stack: Reconstruction of Landscape Evolution Zones (LEZ) from laminated Eifel maar sediments of the last 60,000years. Global and Planetary Change 142, 108–135. https://doi.org/10.1016/j.gloplacha.2016.03.005

Sitzia, L., Bertran, P., Sima, A., Chery, P., Queffelec, A., Rousseau, D.-D., 2017. Dynamics and sources of last glacial aeolian deposition in southwest France derived from dune patterns, grain-size gradients and geochemistry, and reconstruction of efficient wind directions. Quaternary Science Reviews 170, 250–268. https://doi.org/10.1016/j.quascirev.2017.06.029

Stoops, G., 2003. Guidelines for analysis and description of soil and regolith thin sections. Soil Science Society of America Inc.

Stuiver, M., Reimer, P.J., 1993. Extended 14 C data base and revised CALIB 3.0 14 C age calibration program. Radiocarbon 35, 215–230. https://doi.org/10.1017/S0033822200013904

Sun, D., Bloemendal, J., Rea, D.K., Vandenberghe, J., Jiang, F., An, Z., Su, R., 2002. Grain-size distribution function of polymodal sediments in hydraulic and aeolian environments, and numerical partitioning of the sedimentary components. Sedimentary Geology 152, 263–277.

Sun, D., Chen, F., Bloemendal, J., Su, R., 2003. Seasonal variability of modern dust over the Loess Plateau of China. Journal of Geophysical Research: Atmospheres 108. https://doi.org/10.1029/2003JD003382

Sun, Y., Lu, H., An, Z., 2000. Grain size distribution of quartz isolated from Chinese loess/paleosol. Chinese Science Bulletin 45, 2296-2298. https://doi.org/10.1007/BF02886372

Thiel, C., Buylaert, J.-P., Murray, A.S., Terhorst, B., Tsukamoto, S., Frechen, M., Sprafke, T., 2011. Investigating the chronostratigraphy of prominent palaeosols in Lower Austria using post-IR IRSL dating. E&G quaternary science journal 60, 137–152. https://doi.org/info:doi:10.3285/eg.60.1.10

Thirault, E., Ancel, M.J., Ayasse, A., Baradat, A., Deparnay, X., Moreau, C., Rué, M., et al., 2020. Favary, Rousset (Bouches-du-Rhône) (archaeological survey report). Paléotime, Villard-de-Lans.

Thompson, R., Oldfield, F., 1986. Environmental magnetism. Allen and Unwin, London.

Tricart, J., 1952. Paléoclimats quaternaires et morphologie climatique dans le Midi méditerranéen. Quaternary Science Journal 2, 172–188.

Tsoar, H., Pye, K., 1987. Dust transport and the question of desert loess formation. Sedimentology 34, 139–153.

Újvári, G., Kok, J.F., Varga, G., Kovács, J., 2016a. The physics of wind-blown loess: Implications for grain size proxy interpretations in Quaternary paleoclimate studies. Earth-Science Reviews 154, 247–278. https://doi.org/10.1016/j.earscirev.2016.01.006

Újvári, G., Molnár, M., Páll-Gergely, B., 2016b. Charcoal and mollusc shell 14C-dating of the Dunaszekcső loess record, Hungary. Quaternary Geochronology 35, 43–53. https://doi.org/10.1016/j.quageo.2016.05.005

Van Vliet-Lanoë, B., 1985. Frost effects in soils, in: Boardman, J. (Ed.), Soils and Quaternary Landscape Evolution. John Wiley & Sons, New York, pp. 117–158.

Vandenberghe, J., 2013. Grain size of fine-grained windblown sediment: A powerful proxy for process identification. Earth-Science Reviews 121, 18–30. https://doi.org/10.1016/j.earscirev.2013.03.001

Vandenberghe, J., Mücher, H.J., Roebroeks, W., Gemke, D., 1985. Lithostratigraphy and palaeoenvironment of the Pleistocene deposits at Maastricht-Belvédère, southern Limburg, the Netherlands. Analecta 18, 12.

Varennes, G., Ajas, A., Brochier, J.L., Delhon, C., Durand, F., Nicolle, B., Parisot, N., Picavet, R., Roux, L., Vital, J., 2015. Les Croisières, Guilherand-Granges, Ardèche (archaeological survey report). Paléotime, Villard-de-Lans.

Veres, D., Tecsa, V., Gerasimenko, N., Zeeden, C., Hambach, U., Timar-Gabor, A., 2018. Short-term soil formation events in last glacial east European loess, evidence from multi-method luminescence dating. Quaternary Science Reviews 200, 34–51. https://doi.org/10.1016/j.quascirev.2018.09.037

Vermeesch, P., 2012. On the visualisation of detrital age distributions. Chemical Geology 312, 190–194. https://doi.org/10.1016/j.chemgeo.2012.04.021

Vriend, M., Prins, M.A., 2005. Calibration of modelled mixing patterns in loess grain-size distributions: an example from the north-eastern margin of the Tibetan Plateau, China. Sedimentology 52, 1361–1374. https://doi.org/10.1111/j.1365-3091.2005.00743.x

Wacha, L., Rolf, C., Hambach, U., Frechen, M., Galović, L., Duchoslav, M., 2018. The Last Glacial aeolian record of the Island of Susak (Croatia) as seen from a high-resolution grain–size and rock magnetic analysis. Quaternary International 494, 211–224. https://doi.org/10.1016/j.quaint.2017.08.016

Weltje, G.J., 1997. End-member modeling of compositional data: Numerical-statistical algorithms for solving the explicit mixing problem. Mathematical Geology 29, 503–549.

Weltje, G.J., Prins, M.A., 2007. Genetically meaningful decomposition of grain-size distributions. Sedimentary Geology 202, 409–424. https://doi.org/10.1016/j.sedgeo.2007.03.007

Wolf, D., Kolb, T., Alcaraz-Castaño, M., Heinrich, S., Baumgart, P., Calvo, R., Sánchez, J., Ryborz, K., Schäfer, I., Bliedtner, M., 2018. Climate deteriorations and Neanderthal demise in interior Iberia. Scientific reports 8, 1–10. https://doi.org/10.1038/s41598-018-25343-6

Wolf, D., Ryborz, K., Kolb, T., Zapata, R.C., Vizcaino, J.S., Zöller, L., Faust, D., 2019. Origins and genesis of loess deposits in central Spain, as indicated by heavy mineral compositions and grain-size variability. Sedimentology 66, 1139–1161. https://doi.org/10.1111/sed.12539

Wronkiewicz, D.J., Condie, K.C., 1990. Geochemistry and mineralogy of sediments from the Ventersdorp and Transvaal Supergroups, South Africa: Cratonic evolution during the early Proterozoic. Geochimica et Cosmochimica Acta 54, 343–354. https://doi.org/10.1016/0016-7037(90)90323-D

Yaalon, D.H., 1997. Soils in the Mediterranean region: what makes them different? Catena 28, 157–169.

Young, G.M., Nesbitt, H.W., 1998. Processes controlling the distribution of Ti and Al in weathering profiles, siliciclastic sediments and sedimentary rocks. Journal of Sedimentary research 68, 448–455. https://doi.org/10.2110/jsr.68.448

Zens, J., Schulte, P., Klasen, N., Krauß, L., Pirson, S., Burow, C., Brill, D., Eckmeier, E., Kels, H., Zeeden, C., Spagna, P., Lehmkuhl, F., 2018. OSL chronologies of paleoenvironmental dynamics recorded by loess-paleosol sequences from Europe: Case studies from the Rhine-Meuse area and the Neckar Basin. Palaeogeography, Palaeoclimatology, Palaeoecology 509, 105-125. https://doi.org/10.1016/j.palaeo.2017.07.019

Zerboni, A., Trombino, L., Frigerio, C., Livio, F., Berlusconi, A., Michetti, A.M., Rodnight, H., Spötl, C., 2015. The loess-paleosol sequence at Monte Netto: a record of climate change in the Upper Pleistocene of the central Po Plain, northern Italy. J Soils Sediments 15, 1329–1350. https://doi.org/10.1007/s11368-014-0932-2

[dataset] Zickel, M., Becker, D., Verheul, J., Yener, Y., Willmes, C., 2016. Paleocoastlines GIS dataset. CRC806-Database. https://doi.org/10.5880/SFB806.20

Zöller, L., Richter, D., Masuth, S., Wunner, L., Fischer, M., Antl-Weiser, W., 2013. Luminescence chronology of the Grub-Kranawetberg site, Austria. E&G Quaternary Science Journal 62, 127–135.